

6. SITE 1097¹

Shipboard Scientific Party²

BACKGROUND AND SCIENTIFIC OBJECTIVES

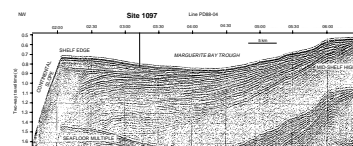
Site 1097 (Fig. F1; also see “Appendix,” p. 24, and Fig. AF1, p. 59, both in the “Leg 178 Summary” chapter) was drilled on the outer continental shelf of the Pacific margin of the Antarctic Peninsula to gain a better understanding of the major changes in the geometry of the glacial prograding wedge.

Site 1097 lies at a water depth of 552 m on the outer shelf, between glacial progradational Lobes 3 and 4 described by Larter et al. (1994, 1997). The site lies 14 km inshore of the continental shelf edge, within the broad trough that connects the shelf edge to the glacially overdeepened inner shelf in Marguerite Bay (Fig. F2A, F2B) and George VI Sound. These areas were conduits for ice draining from a large area of Palmer Land and Alexander Island.

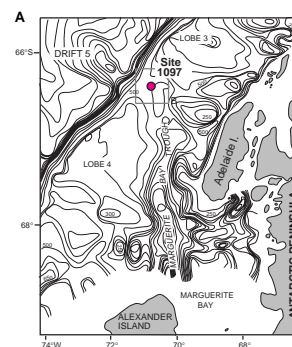
Single-channel and multichannel seismic (MCS) profiles (Bart and Anderson, 1995; Larter et al., 1997) show that the thickness of topset beds of glacial seismic Sequence Groups S1 and S2 of Larter and Barker (1989, 1991a) is reduced to <200 m in the trough (compared to ~ 400 m within the progradational lobes). Sequence Groups S1 and S2 are considered to have been produced by ice-stream transport during ice-sheet grounding to the shelf edge. They are the units whose deposition has determined the main progradation and aggradation of the margin during the Pliocene–Pleistocene (Barker, 1995). The sampling of these units within a progradational lobe was among the drilling objectives on the continental shelf drilling transect.

Beneath Sequence Group S2 is Sequence Group S3, which is more continuous along the margin and parallel-bedded downdip (lacking a clear paleoshelf break). S3 either pinches out or is truncated at its downdip end (on the evidence of seismic reflection profiles). It was therefore considered to record an earlier or transitional stage of glacial deposition on the outer shelf or upper slope, before ice sheets regularly extended to

F1. Location of Site 1097 on single-channel seismic reflection profile PD88-04, p. 23.



F2. Bathymetric map and seismic reflection profiles around Site 1097, p. 24.



¹Examples of how to reference the whole or part of this volume.

²Shipboard Scientific Party addresses.

the shelf break. Sequence Group S3 is more accessible to drilling in an interlobe area than on a lobe, and at this site S3 is clearly separated from collisional tectonics because the age of the ridge crest–trench collision on this sector of the margin is ~17 Ma (Barker and Camerlenghi, [Chap. 2](#), this volume). Below S3 lies Sequence Group S4, across the “uplift unconformity.” The upper boundary of Sequence Group S4 shows erosional unconformity associated with syn- to postcollisional uplift. S3 onlaps this unconformity, marking postcollisional subsidence. The collision and the S3/S4 unconformity were considered here to predate the onset of Antarctic Peninsula glaciation.

The site was spudded in on a highly reflective and irregular seafloor that showed no 3.5-kHz penetration ([Fig. F3](#)) and probably was scoured by iceberg grounding during the Holocene. Drilling at Site 1097 was intended to examine the preglacial and early glacial history of the Antarctic Peninsula margin and to test the hypotheses of the “preglacial” nature of Sequence Group S3 and the uplift/subsidence origin of the S4/S3 boundary by (1) sampling “preglacial” (S3) lithologies and helping test the synchronicity of the conformable S3/S2 boundary along the margin and (2) sampling the (probably tectonic) S3/S4 boundary on the upper continental slope where it should be near-conformable.

OPERATIONS

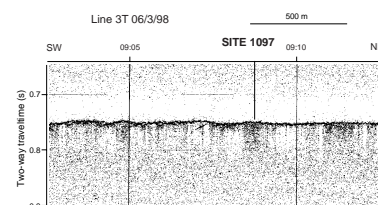
With a following wind and calm seas, we made good time traveling at an average speed of 11.2 kt on the 163-nmi transit from Site 1096 to Site 1097 (scientific prospectus site APSHE-05A). During the transit, 15 icebergs appeared on radar, and we altered the vessel’s course to avoid one large iceberg. The *Polar Duke*, which had left Site 1096 to scout ahead of us, reported that there were six icebergs within 15 nmi of the site location. The *JOIDES Resolution* proceeded directly to site APSHE-05A and dropped a positioning beacon at 0615 hr on 6 March.

Hole 1097A

Because this site did not have sediments suitable for coring with the advanced hydraulic piston corer or extended core barrel, a rotary core barrel (RCB) bottom-hole assembly (BHA) was made up with a new Rock Bit International C-3 bit and a mechanical bit release. Hole 1097A was spudded at 1045 hr on 6 March at an estimated seafloor depth of 551.7 m (563.0 meters below rig floor [mbrf]), 1 m less than the computed precision depth recorder reading. For the next 13 hr, coring at Site 1097 proceeded slower than expected, and core recovery was very low (3.7% for the first 10 cores [[Table T1](#)]) as we attempted to penetrate glacial till containing an abundance of cobbles and boulders.

Meanwhile, six icebergs were being monitored within 6 nmi of the rig. A free-fall funnel was deployed late on 7 March to allow us to reenter the hole, given the likelihood that an iceberg would eventually force us off site. RCB coring resumed and advanced slowly to 164 meters below seafloor (mbsf), where the drill string stuck in the unstable hole. After 45 min of working the pipe and flushing the hole with mud, the pipe was freed. RCB coring resumed and advanced to 246 mbsf (Core 178-1097A-29R), with improving recovery and faster rates of penetration. At 1600 hr on 8 March, we suspended coring operations and pulled the bit to the top of the hole as an iceberg approached. Just after midnight the iceberg drifted within 1 nmi, so the drill string was pulled

F3. 3.5-kHz sub-bottom profile across Site 1097, [p. 26](#).



T1. Site 1097 coring summary, [p. 59](#).

above the seafloor to allow the vessel to maneuver. The iceberg passed within 0.18 nmi of the site at 0415 hr on 9 March (Fig. F4). Because the bit had accumulated 31 hr of rotating time in difficult conditions, we used the waiting time to change it.

At 0710 hr on 9 March, the hole was reentered in <15 min via the free-fall funnel. From 0900 to 1230 hr, the bit was washed and reamed into the unstable formation to 246 mbsf, where circulation was lost after making a connection. The bit was pulled back to 236 mbsf, and attempts were made to clear the drill string and regain circulation. In a last-ditch effort to clear the bit and avoid another round trip of the drill string, a “swab cup” was run in on the wireline to 300 mbrf and then pulled back to the vessel with the drill string connection partially open at the rig floor. The swab cup essentially drained the water in the top 300 m of drill string (spraying the drill floor), which reduced the hydrostatic pressure at the bit. This differential pressure forced formation fluid backup through the bit nozzles and cleared the blockage. The mud pumps were immediately turned on and the pipe flushed clean. As a precautionary move, a bit deplugger was deployed to clear any obstruction that might have been lodged in the throat of the bit.

Coring advanced from 246 to 294 mbsf but then was halted because of excessive vessel heave caused by complex large swells coming from two directions. After sea conditions improved, RCB coring advanced from 294 to 351 mbsf with better recovery (26%) and faster penetration (up to 15 m/hr). This was followed by another 4.3 hr of standby time as ship heave again exceeded 2 m as well as another 5.5 hr of washing and reaming to return to the bottom of the hole.

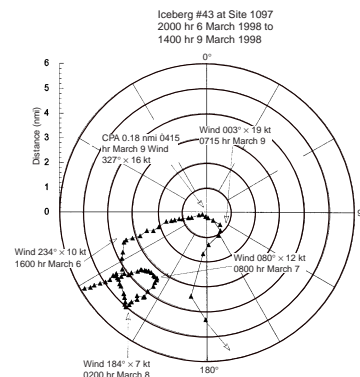
RCB coring had advanced to 436.6 mbsf by 0545 hr on 11 March with 13.6% core recovery overall when operations were again interrupted by the approach of an iceberg. The bit was raised to 400 mbsf while the iceberg remained within range. After the iceberg had passed out of range, the drillers encountered several difficulties attempting to reach the bottom of the hole, including a stuck pipe. At the bottom of the hole, the drillers could not make a connection to retrieve the wash barrel. Because hole conditions were deteriorating, the coring program was terminated, and logging was not attempted. Recovery was 13.6% overall but was significantly greater below 100 mbsf than above.

After the hole was displaced with 85 bbl of 10.5-gallon mud, the drill string was recovered. The bit cleared the seafloor at 1700 hr, and the BHA reached the rotary table at 1800 hr. The drill collar connections were then inspected for any damage incurred as a result of the rough drilling and unusual environmental conditions. The beacon was recovered, and the drilling equipment was secured for transit to Site 1098 by 2100 hr on 11 March. For a summary of drilling at Site 1097, see Table T1, p. 54, in the “Leg 178 Summary” chapter.

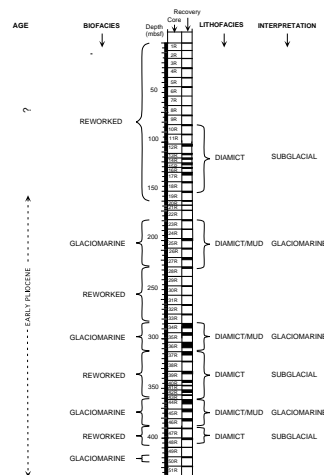
LITHOSTRATIGRAPHY

Poor core recovery at Site 1097 allows a partial picture of the older sedimentary history of the continental shelf to be established (Fig. F5). The total depth of the hole was 436.6 mbsf, and ~57 m of sediment was recovered from the lower part of the hole below ~80 m. Only cobbles were recovered in the upper part of the hole. In the absence of a continuous sedimentary record, lithostratigraphic subdivision is avoided. Nonetheless, a number of glacial and glacially influenced marine sedimentary facies can be identified from recovered core intervals.

F4. Iceberg tracking at Site 1097, p. 27.



F5. Lithofacies, biofacies, age, and inferred environmental setting for Hole 1097A, p. 28.



Subglacial environments are recorded by massive diamicts (defined as clasts supported by a muddy matrix; see “[Lithostratigraphy](#),” p. 3, in the “Explanatory Notes” chapter) that lack any internal structure or bioturbation and contain reworked marine microfauna. These sediments are interpreted as deformation tills produced by the subglacial reworking and transport of marine muds and other sediments below grounded ice. Massive diamicts are the most common facies recovered at Site 1097 (65% of recovered sequence).

Glacially influenced continental shelf environments can also be recognized. Stratified diamicts, which occur in close association with normal and inversely graded diamicts, are interbedded with laminated marine muds containing a well-preserved in situ marine fauna. These diamict facies are interpreted as sediment gravity flows (debrites and turbidites) deposited in a proglacial marine setting characterized by low salinity and high deposition rates, most likely within a few kilometers of an ice margin. Such glaciomarine diamicts are characterized by a soupground ichnofacies assemblage, indicating that diamicts were poorly consolidated during deposition.

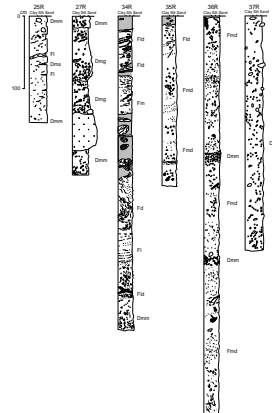
Laminated and massive marine muds, which contain varying numbers of dropstones and are bioturbated, have an in situ marine microfauna, indicating that deposition occurred in both ice-proximal and ice-distal settings. Ice-rafted debris is present throughout; some marine muds contain sufficient ice-rafted debris to generate thin (<30 cm) intervals of massive rainout diamict.

Description of Sediments

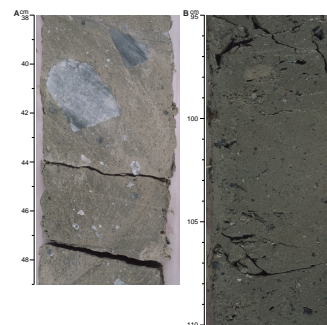
Massive Diamict

Massive diamict (Facies Dmm; Figs. [F6](#), [F7](#)) is the most common facies recovered at Site 1097 comprising ~65% of total recovery. The maximum recovered interval through such facies is 2.95 m (Core 178-1097A-37R). The term *diamict* refers to poorly sorted admixtures of clasts (defined as larger than sand sized) and matrix (see “[Lithostratigraphy](#),” p. 3, in the “Explanatory Notes” chapter). No internal structure or organization can be recognized. Dip angles of elongate clasts >0.5 mm in length were measured from split core surfaces; clasts do not appear to be systematically oriented (Fig. [F8](#)). Matrix grain size varies from silty mud (10%–20% sand, 50%–75% silt, and 10%–40% clay) to sandy silty clay (as much as 30% sand), and clast content varies from clast-rich (>20% gravel) to -poor (10%–20%). The maximum clast size recovered intact in matrix was 6 cm, but it is limited by the throat diameter of the drill bit. The largest boulder drilled was at least 50 cm in diameter; the presence in some poorly recovered intervals of several freshly fractured pieces of the same lithology also indicates large boulders. Clast lithologies include volcanics (basalt, volcaniclastics, andesite, and rhyolite) and plutonic igneous rocks (mafic, granite, and diorite) that are all derived from local Antarctic Peninsula sources (Fig. [F9](#); e.g., Pope and Anderson, 1992). The mineralogy of the sand and silt fraction is dominantly quartz (30%–80%) and feldspar (5%–20%), with minor lithic fragments, mica, and hornblende. Trace amounts of tephra are present in Core 178-1097A-13R, and opaque micronodules (manganese?) of as much as 2% are present in massive diamict facies in Cores 178-1097A-10R and 12R. Matrix color varies from dark gray (5Y 3/1) to green (5GY 3/1). Diamicts are not cemented except for Core 178-1097A-40R, which is indurated and therefore described as diamictite. Massive

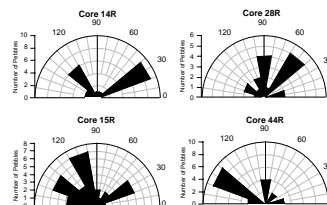
F6. Graphic log from representative cores for Hole 1097A, p. 29.



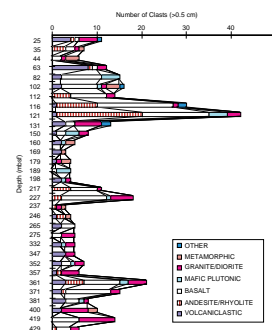
F7. Representative examples of massive diamict lithofacies from Site 1097, p. 31.



F8. Distribution of dip angles of elongate clasts, Hole 1097A, p. 35.



F9. Downhole clast lithology from Site 1097, p. 36.



diamict in Cores 178-1097A-16R and 17R show a horizontal fissility marked by very thin silt laminae (<2 mm thick) (Fig. F7E).

With a single exception (Core 178-1097A-44R; see below), massive diamict and diamictite facies recovered at Site 1097 contain large amounts of reworked and abraded diatoms, foraminifers, and sponge spicules (see “*Biostratigraphy*,” p. 8). In Core 178-1097A-44R, massive diamict is transitional to bioturbated sandy mud with dropstones and shows a poorly defined mottling consisting of patches of lighter colored silt-rich mud (Fig. F6). Sand and granules are concentrated in these mottles, which suggests concentration by burrowing organisms. In contrast, diamict of Core 178-1097A-44R contains well-preserved marine microfossils (see “*Biostratigraphy*,” p. 8).

Graded and Stratified Diamict

These facies show internal structure created by size sorting of clasts and account for 10% (~5 m) of recovered sediments at Site 1097. Beds are between 20 and 50 cm thick and show steep dips and deformation. Graded diamict facies (Facies Dmg; Fig. F6) identifies those beds that show either an upward decrease in clast size (normal grading) or upward increase (inverse grading). Core 178-1097A-27R shows a normally graded diamict bed as much as 40 cm thick (Fig. F6) capped by burrowed muds containing dropstones, well-preserved sponge spicules, and well-preserved marine microfossils. An overlying inverse to normal graded diamict bed rests with a sharp erosive contact on underlying muds and contains a rip-up clast of altered tephra (Fig. F10B, F10C).

Stratified diamict (Facies Dms; Fig. F6) shows slight and nonsystematic variation in matrix texture and clast content, giving rise to weak lamination and crude bedding (e.g., Core 178-1097A-25R; Fig. F11A, F11B). These facies are interbedded with thin beds of mud (as much as 10 cm thick) that contain in situ marine microfauna and flora.

Mud

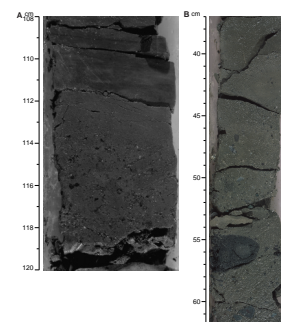
Mud facies account for 25% of recovered sediment at Site 1097. Good sections through muds were recovered in Cores 178-1097A-34R and 36R (Figs. F6, F12). Muds are either weakly laminated or massive and range from silty clay (e.g., Core 178-1097A-36R; 10% sand, 40%–50% silt, and 30%–50% clay) to clayey silt (e.g., Core 178-1097A-34R; 5% sand, 25%–69% silt, and 30%–75% clay). Mud facies contain dropstones and shell fragments and are bioturbated. In Cores 178-1097A-34R to 36R, the content of gravel-sized, ice-rafted clasts in several thin (<10 cm) intervals is sufficiently high (<10%) to warrant description as diamict (e.g., intervals 178-1097A-34R-3, 122–100 cm; 35R-1, 140–150 cm; 36R-2, 80–90 cm; and 36R-3, 15–25 cm; Fig. F6). In Core 178-1097A-34R, laminated and bioturbated muds show broad folds as much as 80 cm in amplitude that are too large to be related to drilling disturbance (Fig. F6).

Facies Interpretation

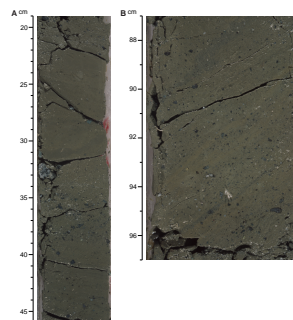
Massive Diamict

Interpretation of massive diamict is not straightforward and relies on contextual information from associated facies and the nature of bed contacts. These data are limited at Site 1097. Massive, matrix-supported diamicts at Site 1097 lack any coherent in situ assemblage of marine

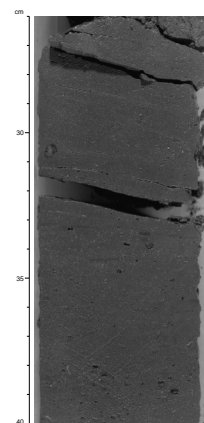
F10. Graded diamict facies at Hole 1097A, p. 37.



F11. Stratified diamict facies from Hole 1097A, p. 39.



F12. Weakly laminated silty clay with ice-rafted clasts, interval 178-1097A-34R-1, 26–40 cm, p. 40.



microfauna and flora but contain large amounts of abraded and fragmented material. The lack of any in situ microfossils, internal stratification, and bioturbation appears to preclude an origin by the rainout of suspended sediment and ice-rafted debris. A debris-flow (debrite) origin is possible, although diamicts are unstructured and do not show the chaotic bedding or flow fabric seen in debrites at Site 1103 (see “**Lithostratigraphy**,” p. 5, in the “Shelf Transect [Sites 1100, 1102, and 1103]” chapter). Massive diamicts at Site 1097 are probably of subglacial origin, given the presence of reworked and abraded marine microfossils. Diamicts are likely to have been deposited as deformation till where marine sediment has been reworked subglacially as a “soft” or deforming bed (e.g., Boulton, 1990; Fig. F13). Subglacial incorporation of pre-existing sediment has been widely invoked in explaining massive diamict with reworked marine microfossils on glaciated continental surfaces and shelves (e.g., Boulton, 1996; Clark et al., 1996). Fissile and weakly stratified diamict found as thin (30 cm) intervals within massive diamict in Cores 178-1097A-16R and 17R (e.g., Fig. F7E) may record subglacial shear or limited sorting by subglacial water; on the other hand, such fissility could be the result of unloading and swelling after coring.

Contextual information is available for massive diamicts in Cores 178-1097A-36R, 35R, and 44R. These diamicts lack sharp bed bases and tops and are transitional to bioturbated muddy sands with ice-rafted clasts (Facies Fmd; Fig. F6). They also contain intact microfaunal and floral assemblages indicating deposition in shallow water (100–300 m) (see “**Biostratigraphy**,” p. 8). Burrows with poorly defined walls are also present, indicating soft sediment at the time of burrowing. Because of these characteristics, massive diamicts in Core 178-1097A-44R are interpreted as rainout facies produced by suspension settling of mud with coarser material rafted in by floating ice. Variation in the flux of ice-rafted debris through time gives rise to transitions from mud with sufficient numbers of clasts to be identified as diamict (Facies Dmm), to mud with isolated ice-rafted clasts (Facies Fmd).

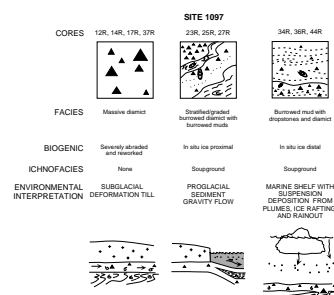
Graded and Stratified Diamict

Stratified diamict and graded diamict (Facies Dms and Dmg) form distinct beds associated with marine muds containing well-preserved marine microfauna and flora (e.g., Core 178-1097A-25R; Figs. F6, F11, F12). These diamict facies are interpreted as sediment gravity flows (debrites). Interbeds of mud in Core 178-1097A-25R, for example, probably record pauses between debris flows, which allow mud accumulation. Graded facies (Facies Dmg; Fig. F6) result from turbulent downslope flow resulting in the segregation of different size fractions (see Walker, 1992). An ice-proximal marine setting for stratified and graded diamicts is suggested by marine microfossils present in diamict and associated muds. The microfossils denote deposition within a few kilometers of a glacier terminus in an area of high sedimentation and reduced salinity caused by meltwater input (see “**Biostratigraphy**,” p. 8). Given this setting, downslope resedimentation is likely to have been near to the ice front where subglacial debris (deformation till; see above) was released and moved downslope by mass flow (Fig. F13). Consequently, stratified and graded diamict facies are recognized as glaciomarine in origin.

Muds

Massive muds accumulate in a wide range of settings on glaciated continental shelves. The most common depositional process is suspen-

F13. Summary of facies recovered at Site 1097, p. 41.



sion settling of fines carried by meltwater plumes. Tidal and bottom-current interaction with plumes generates laminated muds (e.g., Griffith and Anderson, 1989; Domack, 1990). Mud recovered in Cores 178-1097A-36R and 44R contains marine biota indicating water depths between 100 and 300 m and salinity characteristic of an open shelf distal to ice margins (see “[Biostratigraphy](#),” p. 8). Muds are bioturbated and contain variable quantities of ice-rafted debris including thin intervals of diamict (Fig. [F6](#)). Core 178-1097A-44R contains a thick (3 m) section of rainout diamict (see above) produced by ice rafting and suspension settling of mud (see above and Fig. [F13](#)). The deformed mud in Core 178-1097A-34R (Fig. [F6](#)) may result from iceberg scour of the substrate or downslope slumping.

Depositional Setting and Environmental Interpretation of Site 1097

Because of an inability to collect continuous stratigraphic information at Site 1097, recovered facies provide a partial picture of glacial and glacially influenced deposition on the continental shelf. Inferred environments range from subglacial through glaciomarine to open-marine shallow shelf (Fig. [F13](#)).

The lithostratigraphy at Site 1097 can be divided into two thick intervals with differing characteristics (Fig. [F5](#)). The lower, below ~180 mbsf, shows an alternation between subglacial conditions, when grounded ice extended across the shelf, and glaciomarine conditions, when the shelf was partially free of grounded ice and Site 1097 lay seaward of the ice margin. Biofacies data from the upper part of Site 1097, above ~155 m, indicate that subglacial conditions were dominant throughout this upper interval. This possibility suggests a major change in style of glacial deposition along the Antarctic continental margin (see “[Seismic Stratigraphy](#),” p. 18). This may have implications for changing ice volumes through time.

Within the glaciomarine intervals at Site 1097, weakly bioturbated, massive, and laminated muds with high ice-rafted debris content suggest influxes of meltwater, suspended sediment, and icebergs to Site 1097 during early Pliocene(?) time (Fig. [F5](#)). These deposits suggest a subpolar or temperate glacier regime and the release of meltwater plumes derived from subglacial meltwaters that intercept easily erodible marine sediment or deformation till. The biogenic component of the mud within these glaciomarine intervals is generally <10%, which is much less than the biogenic component of sediments accumulating on the modern Antarctic Peninsula shelf. For example, many of the cores described by Pope and Anderson (1992) are capped by diatomaceous muds, and the upper part of cores analyzed by Pudsey et al. (1994) contain from 30% to 60% diatoms. The low values recorded in muds at Site 1097 could reflect an influx of fine-grained, meltwater-derived, terrigenous sediment as well as environmental factors such as reduced salinity.

Glacial Processes and Depositional Models

Intervals of expanded glaciation, when grounded ice reached the shelf edge, are recorded at Site 1097 by massive diamicts that are interpreted as deformation tills. During glacier expansion, fine-grained marine sediments within fjords and inner shelf basins were probably reworked subglacially and transported below ice streams to the outer

shelf. The recovery of deformation till at Site 1097, if correctly interpreted, is important because these are the first such sediments to be recovered from the Antarctic continental margin. Work on Pleistocene mid-latitude ice sheets has shown that the ice-sheet margins rested on “soft” deformable beds giving rise to a low surface profile and fast ice flow (“streaming”). It has been suggested that such conditions existed on the Antarctic Peninsula shelf (e.g., Pudsey et al., 1994; Bart and Anderson, 1995), and there has been much discussion of depositional mechanisms (Alley et al., 1989; Vanneste and Larter, 1995). To date, such facies have not yet been described anywhere along the continental margin of Antarctica. The occurrence of drumlin and flute fields on the shelf adjacent to Site 1097 (Pudsey et al., 1994) may be further evidence of “soft bed” conditions below ice sheets extending onto the shelf (e.g., Boulton and Hindmarsh, 1987; Boyce and Eyles, 1991).

BIOSTRATIGRAPHY

One hole was drilled at Site 1097, with 13.6% core recovery. Radiolarians, diatoms, and foraminifers were all present at this site, with abundances of each varying by sample (Fig. F14). Because of the glaciomarine nature of the sediments, reworking of microfossils is prevalent in most samples. Most of the marine muds within the diamicts in Hole 1097A, however, appear to have been deposited during interstitial conditions within the early Pliocene. The upper 125 m (Cores 178-1097A-1R through 15R) are reworked diamict sediments essentially barren of microfossils. Below 125 m (Core 178-1097A-16R), microfossils occur in intervals alternating with barren diamicts.

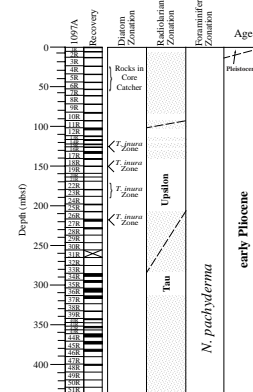
Diatoms

Samples 178-1097A-1R-CC and 2R-CC comprised rocks with some fine-grained sediment (diamict matrix) containing fragments of diatoms. The only age-diagnostic species were *Fragilariopsis kerguelensis* (present–3 Ma), *Denticulopsis simonsenii* s.l. (Miocene), and *Denticulopsis delicata* (Miocene). The obvious reworking of older sediment (concluded through observation of species of mixed ages and fragmentation of valves) and the low total abundance and diversity of diatoms recovered preclude any possible age inference (Fig. F15).

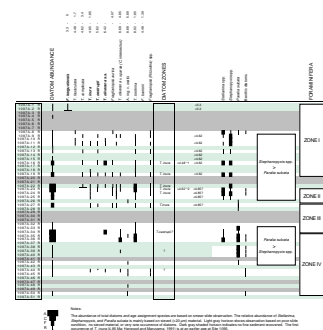
Only rocks, with no fine-grained sediments, were recovered from Cores 178-1097A-3R through 7R. The fine-grained diamict matrix of Sample 178-1097A-8R-CC contains a non-age diagnostic assemblage, consisting of *Paralia sulcata*, *D. simonsenii* s.l., *D. delicata*, *Actinocyclus ingens*, *Thalassiosira complicata*, *Coscinodiscus* spp., and *Nitzschia/Fragilariopsis* spp. The ages of these species range from Miocene to Pliocene, with most extending over a long time period. The absence of middle to late Pliocene and Pleistocene diatom species such as *Fragilariopsis baronii* (4.48–1.39 Ma), *Fragilariopsis interfrigidaria* (3.8–2.67 Ma), *F. kerguelensis* (3.3 Ma to Holocene), *Thalassiosira insigna* (3.4–2.57 Ma), and *Thalassiosira vulnifica* (3.17–2.28 Ma) suggest an early Pliocene age for the source sediment.

Pliocene diatoms, including *Thalassiosira torokina*, *Thalassiosira oestrupii*, *Thalassiosira oliverana*, and fragments of *Thalassiosira fasciculata*, occur within Samples 178-1097A-9R-CC through 11R-CC, where diatoms are more common than in overlying sediments. Published age ranges of some of the species observed help to constrain the age of dep-

F14. The occurrence of diatoms, radiolarians, and planktonic foraminifers at Site 1097, p. 42.



F15. Diatom stratigraphy at Site 1097, p. 43.



osition of this material (first occurrence [FO] of *Thalassiosira inura*, 4.85 Ma; FO of *T. complicata*, 4.62 Ma; FO of *T. fasciculata*, 4.48 Ma; FO of *Fragilariopsis praeinterfrigidaria*, 4.85 Ma). Using last occurrences in glacial sediments is rarely an option because of common reworking. Thus, the only age that can be determined from this sediment is an age younger than the FO of the youngest of the species observed (Figs. F14, F15).

Cores 178-1097A-16R, 19R, 23R, and 27R contained a diverse assemblage typical of the *Thalassiosira inura* Zone including *T. inura*, *T. oestrupii*, *T. torokina*, *Fragilariopsis aurica*, *F. praeinterfrigidaria*, *Fragilariopsis praecurta*, *Actinocyclus karstenii*, and *Nitzschia reinholdii*. With the inclusion of *T. inura* (the characteristic period assemblage) and the exclusion of *F. barronii* (the FO of this species marks the upper boundary of the *T. inura* Zone), it is likely that these sediments are from the *T. inura* Zone (Fig. F15).

Diatoms are rare with poor to moderate preservation below Core 178-1097A-37R. The neritic diatom species, *Paralia sulcata*, is dominant (more than 80%) in core-catcher samples from Cores 178-1097A-37R through 41R (Fig. F15). Overall diatom abundance and preservation decrease below this, but numbers of benthic diatoms increase slightly in samples below Core 178-1097A-41R as compared with overlying sediments.

The occurrence of the well-preserved epiphytic diatom species *Arachnoidiscus ehrenbergii* in sieved material (>63 μm) of Samples 178-1097A-42R-CC and 44R-CC, along with increasing numbers of benthic diatoms (including *Cocconeis* spp., *Navicula* spp., *Gramatophora* spp., and *Delphineis* spp.) in core-catcher samples below Sample 178-1097A-42R-CC, suggests a shallowing sequence to the bottom of the hole.

Figure F15 illustrates the ranges and abundances of selected diatom species in Hole 1097A. The samples that can be assigned to a particular zone (all within the *T. inura* Zone) are indicated. The change from many *Stephanopyxis* spp. in the upper part of the hole to a *Paralia sulcata* and benthic diatom species peak in the lower part of the hole is also shown.

Radiolarians

Radiolarians were rare in core-catcher samples from Hole 1097A, and skeletons were broken. One reworked Cretaceous specimen was found in Sample 178-1097A-19R-CC. Age assignments were difficult because of the reworked nature of the sediments and the low abundances and poor preservation of radiolarians. Species typical of shelf environments (e.g., *Spongotrochus glacialis*, *Spongopyle osculosa*, and *Porodiscid* spp.) dominated the assemblages. The youngest marker species encountered was *Acrosphaera cylindrica* in Sample 178-1097A-10R-CC (92.1 mbsf), indicating an age of at least 0.610 Ma (Fig. F14). Species consistent with an age in the Upsilon Zone (*Helotholus vema*, *Prunopyle titan*, and *Lampromitra coronata*) were sporadic from Sample 178-1097A-12R-CC (111.5 mbsf) to 25R-CC (207.7 mbsf). The upper limit of the Upsilon Zone is placed in the barren interval of Core 178-1097A-11R (92.1–101.8 mbsf). The absence of *H. vema* below Sample 178-1097A-34R-CC (293.9 mbsf) suggests that the age of the sediment falls within the Tau Zone (older than 4.580 Ma). The boundary between the Upsilon and Tau Zones could be in the barren interval from Sample 178-1097A-26R-CC (217.3 mbsf) to 34R-CC (293.9 mbsf) (Fig. F14).

Foraminifers

At Site 1097 all core-catcher samples, plus 10 additional core samples, were processed for foraminifers. Benthic foraminifers were present in all but five samples. *Neogloboquadrina pachyderma* sinistral was observed in Samples 178-1097A-36R-2, 85-87 (305.8 mbsf), and 44R-CC (365.4 mbsf). In addition, most samples examined contained reworked foraminifers and other biogenic components. Most reworked biogenic material is recognizable by dark discoloration and poor preservation. The amount of reworked biogenic materials observed in the sand fraction suggests that all samples record marine conditions that are near to, or beneath, a glacial ice front (Osterman, 1984). Even the most marine benthic foraminifer assemblage (Biofacies C; Table T2) implies conditions near grounded ice. Benthic foraminifers can provide no information about the previous existence or extent of an ice shelf at this site or farther inshore.

Three qualitative environmental biofacies are defined for Site 1097 (Table T2). It is important to recognize that there is great variability in the fauna preserved in these sediments. The benthic foraminifer and sedimentological records suggest rapid changes within small intervals of cored sediment. For example, replicate analyses of core-catcher Sample 178-1097A-44R-CC produced different values of foraminifer abundance and diversity, which implies that there were variable environments of deposition at this site within a small geographic area or time. The biofacies are defined broadly, however, and both analyses of Sample 178-1097A-44R-CC fall within the definition of Biofacies C.

Biofacies A consists predominantly of a reworked assemblage of benthic foraminifers. These samples contain <12 robust, yellow-colored foraminifer specimens often broken or filled with sediment, indicating transport and reworking. Also, this assemblage often contains additional worn, discolored, and replaced biogenic matter including *Inoceramus* prisms, mollusk shell fragments, and echinoderm spines and shell fragments. Benthic foraminifers of this biofacies consist almost exclusively of *Globocassidulina subglobosa* and *Cassidulinoides parkerianus*. This biofacies is believed to record glacial transport within a subglacial environment.

Biofacies B contains poor to moderately well-preserved and slightly more abundant foraminifers ranging from 12 to 30 foraminifers per sample. Better preservation of the foraminifers implies minimal glacial transport, but the lower numbers indicate less-marine conditions. Biofacies B is believed to record lower salinity shallow-water conditions or dilution of the foraminiferal fauna by higher sedimentation rates in an environment proximal to a glacier front. The low diversity of species (<5) indicates a lowered salinity.

Biofacies C consists of better preserved specimens of foraminifers, often in association with additional well-preserved, white, biogenic material of mollusk shells, sponge spicules, echinoderm spines, and fragments. Preservation of foraminifers in this facies is mixed, with both well-preserved and yellow reworked specimens, sometimes in the same sample. In five of the seven samples of this biofacies, the number of foraminifers ranges from 31 to 250 (¼ split) and the number of species from six to 13. The other two samples are placed in this biofacies based on excellent preservation of the foraminifers and associated biogenic material (fresh mollusk fragments). This biofacies is interpreted to record shallow-water marine conditions not exceeding a depth of 500 m.

T2. Benthic foraminiferal biofacies of shipboard samples from Site 1097, p. 60.

Using these biofacies, Hole 1097A can be divided into four zones (Table T2). Biofacies A predominates in the upper 151 mbsf of Zone I. This interval, containing reworked marine components, is interpreted to be a subglacial till (see also “Lithostratigraphy,” p. 3). Zone II, from Samples 178-1097A-23R-1W, 42–44 cm (179.32 mbsf), to 26R-CC (208.91 mbsf), contains all three biofacies. It is believed, however, to record an episode of more-marine sedimentation with glaciers nearby, which agrees with the diatom analysis of this hole. Zone III, from 218.3 to 287.7 mbsf, contains poor and rare assemblages of Biofacies A and may record an additional episode of subglacial conditions. Zone IV, in the lowest portion of Hole 1097A (288.8 mbsf to the bottom of the hole), includes Biofacies A, B, and C. It also records episodes of more-marine conditions alternating with episodes of low salinity and/or higher sedimentation rates that suggest closer proximity to a glacial front. The washed foraminifer samples in this lower zone contain the large diatom *Arachnoidiscus ehrenbergii*. This diatom lives on shallow-water marine grasses and presently is found in the shallower regions of the Antarctic Peninsula (Krebs, 1977). In addition, this diatom was recovered at the nearshore Sites 1098 and 1099. This supports a shallower continental shelf interpretation for Zone IV with respect to the other zones.

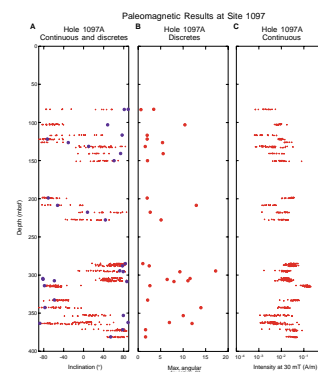
The benthic foraminifers of the more-marine intervals of Site 1097 are similar to Pliocene assemblages recorded in other areas of the Antarctica shelf. *Ammonia* spp., found throughout Zone IV, is reported to be restricted to the early to middle Pliocene in Deep Sea Drilling Project Site 273 (Hayes, Frakes, et al., 1975). Its occurrence in the Pecten Gravels of Wright Valley is bracketed by volcanic dates of 2.5 and 3.8 Ma (Webb, 1974). This species also occurs in Dry Valley Drilling Project Holes 10 and 11 in Taylor Valley (Ishman and Webb, 1988). Although all these faunas are similar to Site 1097, the diversity is much greater in the Ross Sea area (10 to 43 species), possibly because of deeper water in that area. The water depth of the Pliocene Taylor Fjord is estimated to have been 500–800 m. The lower diversity at Site 1097 suggests that the water depth here was <500 m in Zone II, the most marine interval, and <200 m in Zone IV.

PALEOMAGNETISM

Split-Core Measurements

Archive halves of 27 of the 58 RCB sections recovered (excluding core catchers) at Site 1097 were measured using a 5-cm measurement interval (Fig. F16). From Core 178-1097A-17R to the bottom of the hole, the sensor velocity was decreased from 15 to 10 cm/s to avoid saturation of the magnetometer electronics. This saturation results from high variations of the magnetic flux (flux jumps) induced by the rapid motion of highly magnetized material past the sensor. Sections of cores containing pebbles and cobbles (dropstones or rocks from glacial units) were not measured because their magnetization is unrelated to the ambient geomagnetic field at the time of deposition and cannot be used for constructing a magnetostratigraphic record. In addition, many dropstones have a very high intensity of magnetization, which causes flux jumps in the cryogenic magnetometer.

F16. Inclination of the magnetization vector, p. 44.



Discrete Samples

Measurement of discrete samples from the working halves of cores and subsequent data analysis followed the methods described in “**Paleomagnetism**,” p. 16, in the “Site 1095” chapter. Stepwise alternating field (AF) demagnetization of samples revealed that the drill-string overprint was dominantly vertically downward, showing the same behavior as that observed at Site 1095 (see “**Paleomagnetism**,” p. 16, in the “Site 1095” chapter). The drill-string overprint was mostly or wholly removed by partial AF demagnetization of the natural remanent magnetization (NRM) at the 10-mT level. Of the 28 samples measured (Fig. F16), 12 had no stable direction of magnetization (Fig. F17). These samples are mainly from Cores 178-1097A-10R through 18R and 40R through 44R, which were identified as diamicts (See “**Lithostratigraphy**,” p. 3). The magnetization in the diamicts appears to be controlled by coarse-grained magnetic minerals ($>10\ \mu\text{m}$ for magnetite), which are inherently poor magnetic recorders and typically give no stable magnetization direction.

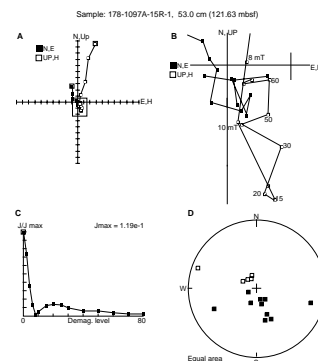
Within a multidomain grain ($>10\ \mu\text{m}$ for magnetite), the magnetic moments organize into many regions such that the vector sum of all the moments, and hence the magnetostatic energy, is minimized. This inherent property of multidomain magnetic minerals precludes their recording a depositional remanence. A depositional remanence is acquired through the torque exerted by the Earth’s magnetic field on the magnetization of a magnetic mineral. Large multidomain grains whose magnetization is extremely small experience a very weak torque, which is not sufficient to overcome gravitational effects and align the grain’s magnetization with the geomagnetic field.

Stable directions were found in the finer grained intervals of Cores 178-1097A-19R through 28R, 34R through 39R, and 45R through 46R. Of the 16 samples with stable directions, eight had weak intensities and dropped into the noise level of the cryogenic magnetometer at the 40- or 50-mT AF demagnetization step. These directions were only stable between 10 and 40 mT and typically had a shallow inclination, which is inconsistent with what is expected for a high-latitude site (Fig. F18). Two of these samples, 178-1097A-27R-1, 34 cm, and 17R-1, 69 cm, were taken from sediments that were identified as a debris flow and a weakly stratified deformation till, respectively (see “**Lithostratigraphy**,” p. 3). The shallow inclinations observed in these samples could be the result of the depositional process and may not reflect the geomagnetic field direction. Only eight of the 28 subsamples had strong intensities and steep inclinations. These samples came from ice-proximal glacial marine lithologies (Fig. F19) (see “**Lithostratigraphy**,” p. 3).

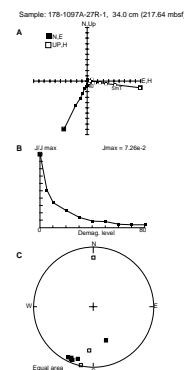
Magnetostratigraphy

Several complications make the construction of a magnetostratigraphy impossible. First, the nature of deposition of diamicts, the main lithology (see “**Lithostratigraphy**,” p. 3), is probably erratic instead of continuous through time. Second, it is unclear how a diamict would acquire a depositional remanence: deposition of magnetic particles within a diamict unit should be controlled by ice flow and gravity flows within the massive unit, instead of orientation of particles by the geomagnetic field as they fall through the water column (the standard depositional remanence mechanism).

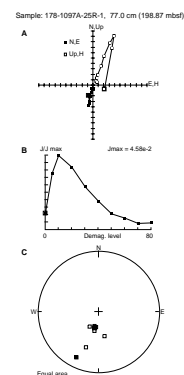
F17. Orthogonal projection of the end-points of the remanence vector for Sample 178-1097A-15R-1, 53.0 cm (121.63 mbsf), 53 cm, p. 45.



F18. Orthogonal projection of the end-points of the remanence vector for Sample 178-1097A-27R-1, 34 cm, p. 46.



F19. Orthogonal projection of the end-points of the remanence vector for Sample 178-1097A-25R-1, 77.0 cm (188.87 mbsf), 77 cm, p. 47.



Finer grained lithologies (silty clays instead of diamicts) at Site 1097 give stable paleomagnetic results, but the occurrences of these lithologies were sparse. A hiatus between each change in lithology is possible, with the time gap possibly being significant relative to the length of geomagnetic reversals. A more severe interpretation limitation comes from the large gaps in recovery. The gaps are 1–10 times the size of the recovered intervals. A smaller problem is that the position of the recovered core is also not known within the cored interval. Cores 178-1097A-10R though 46R may give a sequence of normal and reversed polarities, but this oversimplified interpretation ignores the complications discussed above. Furthermore, even with a short sequence of reversals in an undated stratigraphic section with unknown sedimentation rates, a unique interpretation is impossible. The erratic nature of deposition on the continental shelf, the inability of coarse-grained magnetic minerals (common in diamicts and diamictites) to record the paleomagnetic field, the lack of age constraints, and sparse recovery all prevent construction of a meaningful magnetostratigraphy.

ORGANIC GEOCHEMISTRY

As required by safety regulations, headspace gas analyses were performed immediately upon recovery of each sediment core at Site 1097. Inorganic carbon concentrations were measured on 23 samples, and elemental analyses were performed on a subset of nine samples.

Volatile Hydrocarbons

As a routine procedure for safety and pollution prevention, hydrocarbon gases were monitored while coring Hole 1097A. Methane concentrations varied from 1500 to 76,000 ppm, and ethane concentrations varied from 0 to 14 ppm. Trace amounts of propane and ethylene were also measured in some samples (Table T3). Methane concentrations are similar to those obtained from comparable depths at Site 1096, whereas ethane concentrations are lower, resulting in a higher methane:ethane ratio. With regard to safety and pollution, the risk from coring was negligible at Site 1097.

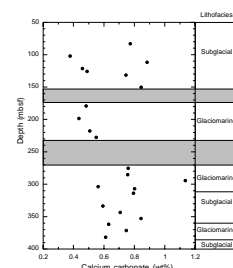
Inorganic Carbon and Elemental Analysis

In intervals of relatively good recovery, one sample per core was analyzed for inorganic carbon (Table T4). Sediment with a high content of coarse sand and gravel was sieved through a 710- μ m mesh before analysis. The sediment at Site 1097 consists of alternating glaciomarine, subglacial, and reworked sequences, on the basis of lithofacies and biofacies (see “Biostratigraphy,” p. 8, and “Lithostratigraphy,” p. 3). Calcium carbonate concentrations vary over a low and relatively narrow range from 0.4 to 1.1 wt%. The upper interval (80–150 mbsf) of subglacial sediment shows somewhat scattered carbonate concentrations (Fig. F20). The glaciomarine facies of the middle interval (170–230 mbsf) corresponds to low carbonate concentrations and may reflect enhanced carbonate dissolution. Carbonate data from the lower interval (270–390 mbsf) do not vary much between the alternating glaciomarine and subglacial lithofacies identified in the lithostratigraphy; however, slightly higher carbonate values in this interval may indicate less dissolution and higher local productivity of shallow-water calcare-

T3. Volatile hydrocarbons measured at Site 1097, p. 61.

T4. Summary of inorganic carbon, carbonate, and elemental analyses for Hole 1097A, p. 62.

F20. Calcium carbonate concentrations for Hole 1097A, p. 48.



ous organisms. In fact, the highest carbonate value corresponds to a glaciomarine facies that also contains the highest abundance of foraminifers.

Nine samples from the glaciomarine intervals were selected for elemental analyses of total organic carbon. Measured concentrations (Table T4) vary from 0.16 to 0.61 wt%, with the highest values occurring in the middle interval (170–230 mbsf).

INORGANIC GEOCHEMISTRY

Interstitial Water Chemistry

We squeezed four whole-round core samples for interstitial water from depths between 280 and 380 mbsf at Site 1097 (Table T5). Poor core recovery and the presence of large rocks in most depth intervals limited the availability of suitable sample material. Furthermore, one of the four samples (Sample 178-1097A-42R-2, 114–124 cm) yielded only 10 mL of interstitial water; another (Sample 178-1097A-45R-1, 140–150 cm) yielded only 5 mL because of the coarse-grained, semilithified nature of the recovered sediment. We consequently could not perform a complete suite of analyses for all samples, and we provide here a necessarily limited interpretation of the results.

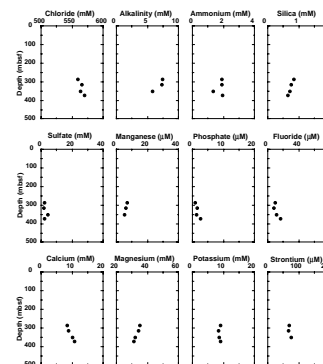
In general, the interstitial water chemistry (Fig. F21) fits the pattern expected for terrigenous sediments buried to a few hundred meters depth with relatively small amounts of biogenic components. Low concentrations of sulfate, manganese, and iron indicate that these sediments lie below the sulfate reduction zone. Maximum alkalinity and ammonium concentrations (7.4 and 1.9 mM, respectively) approach those observed at comparable depths in the rise sediment (Sites 1095 and 1096) and confirm that decaying organic matter influences the shelf sediment. Phosphate concentrations remain quite low (<3 μM), however, in the sampled depth range, and fluoride also reaches low concentrations (<20 μM) relative to seawater (70 μM). These factors suggest that fluoride uptake, perhaps through apatite precipitation, occurs somewhere in the upper sediment column. The range of dissolved silica concentrations (0.64–0.84 mM) exceeds that of normal seawater but remains below the solubility limit of opal-A (~1.1 μM ; Kastner et al., 1977). Thus, although some silica dissolution has occurred, the shelf sediment apparently does not contain an excess of opal. Also, calcium concentrations deviate only slightly from seawater, perhaps not a surprise given the nearly carbonate-free composition of the shelf sediment (see “Organic Geochemistry,” p. 13). Magnesium, potassium, and strontium concentrations lie significantly below seawater values and indicate that the shelf sediment acts as a sink for these elements, probably through clay mineral reactions.

X-Ray Diffraction Mineralogy

Five samples were analyzed for their bulk and clay mineralogy by X-ray diffraction. The two shallowest samples (from 73 and 132 mbsf) represent glacial till, and the three deeper samples (from 218, 295, and 362 mbsf) represent glacial marine sediment that contains varying amounts of ice-rafted debris (see “Lithostratigraphy,” p. 3). These shelf deposits contain the same mineral assemblage as that identified on the nearby continental rise (Sites 1095 and 1096): primarily quartz, feldspars, and a

T5. Results of interstitial water analyses for Hole 1097A, p. 63.

F21. Profiles of interstitial water chemistry from Hole 1097A, p. 49.



blend of clays consisting of chlorite, illite, and a mixed-layer clay as well as traces of amphibole. However, the shelf sediment contains significantly more feldspar and less clay relative to quartz. The average intensity of the 3.19-Å plagioclase peak equals 66% of the 3.34-Å quartz peak (Table T6), compared to only 40% for Sites 1095, 1096, and 1101 (see Table T32, p. 162, in the “Site 1095” chapter; Table T26, p. 133, in the “Site 1096” chapter; and Table T2, p. 65, in the “Site 1101” chapter), whereas the 7-Å chlorite peak averages only 9% of the quartz peak at Site 1097, compared to 12% at the rise sites. Also, average chlorite/illite ratios are highest in the shelf sediments (Table T7; Fig. F22). The one exception to these observations is the glaciomarine mud from 218 mbsf, which has feldspar and clay contents similar to those observed in the rise sediments. The richer feldspar and poorer clay content of the shelf sediment may reflect factors such as larger average grain size and closer proximity to sediment sources. Alternatively, some of these differences may reflect a different provenance for a part of the rise sediment.

X-Ray Fluorescence and Trace-Element Chemistry

Trace-element concentrations were measured by X-ray fluorescence on splits of all five samples that were analyzed by X-ray diffraction (Table T8). These samples have similar trace-element compositions, although the sample from 218 mbsf generally has higher concentrations of most elements, perhaps because of its higher clay content. The concentrations of some elements in the shelf sediment differ from those observed in the rise sediment (Sites 1095 and 1096). Barium concentrations reach as low as any measured at the rise sites and presumably reflect a purely detrital signal, with little or no Ba deposited as a result of high biological productivity on the shelf. Most other trace elements, particularly Rb and Cr, have lower concentrations than were measured in most samples from Sites 1095 and 1096. Like the XRD data (see “X-Ray Diffraction Mineralogy,” p. 14), these results suggest a different provenance for part of the rise sediment.

PHYSICAL PROPERTIES

Whole-Core Measurements

Multisensor Track (MST)

Recovery was limited at Site 1097, which severely affected physical properties data quality and distribution. Measurements are therefore scattered and discontinuous throughout the drilled interval. Natural gamma-ray (NGR) activity, magnetic susceptibility, and gamma-ray attenuation porosity evaluator (GRAPE) density were measured on whole-round sections (see “Physical Properties,” p. 20, in the “Explanatory Notes” chapter). All measurements were made down to near the base of Hole 1097A to a depth of ~400 mbsf.

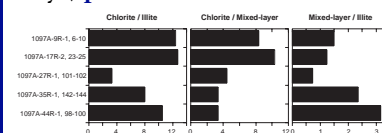
Magnetic Susceptibility

Whole-core magnetic susceptibility was measured at 2-cm intervals (averaged over 2 s). The raw data are provided [on CD-ROM and the](#)

T6. Relative intensities of selected X-ray diffraction peaks from bulk mineral samples of Site 1097 sediments, [p. 64](#).

T7. Relative intensities of selected X-ray diffraction peaks from clay mineral samples of Site 1097 sediments, [p. 65](#).

F22. Ratios between X-ray diffraction intensities of selected peaks for chlorite, illite, and mixed-layer clays, [p. 50](#).



T8. Trace-element chemistry of bulk sediment in Hole 1097A, [p. 66](#).

[World Wide Web](#) and presented in Figure F23. The data show no obvious correlation with core lithologies.

GRAPE Bulk Density

Density was measured by gamma-ray attenuation at 2-cm intervals (averaged over 2 s at each point). The raw data are [on CD-ROM and the World Wide Web](#) and appear in Figure F23. The data show no apparent correlation with lithostratigraphic variation. Plots of GRAPE density vs. magnetic susceptibility reveal no distinct populations.

Natural Gamma Radiation

Whole-core natural gamma-ray emissions (averaged over 15 s) were counted at 15-cm intervals. The raw data are provided [on CD-ROM and the World Wide Web](#) and presented in Figure F23. There is evidence for a broad decrease in the NGR signal down the cored section.

Split-Core Measurements

Index Properties

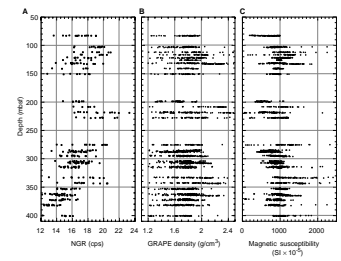
Gravimetric and volumetric determinations of index properties were made on 30 samples from Hole 1097A. One sample was taken every first and third section per core, where possible. Wet mass, dry mass, and dry volume were measured and, from these measurements, percentage water weight, porosity, dry density, bulk density, and grain density were figured (see [“Physical Properties,”](#) p. 20, in the [“Explanatory Notes”](#) chapter; Fig. F24; raw data [on CD-ROM and the World Wide Web](#)).

A positive correlation exists between GRAPE density and density from index properties (Fig. F24A). The index properties grain density shows a weak increase with depth. Porosity decreases below 150 mbsf, which probably reflects the increasing overburden.

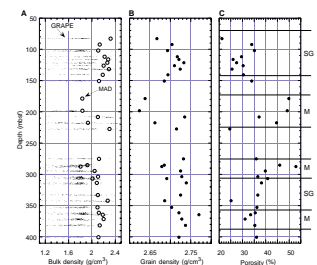
The low-porosity interval between 80 and 150 mbsf matches a lithostratigraphic interval interpreted as subglacial diamict containing reworked marine biogenic material (see [“Lithostratigraphy,”](#) p. 3, and Fig. F24C). Given the much higher porosity in the glaciomarine material between 180 and 225 mbsf, the low porosity above probably reflects subglacial shear consolidation of ~20% within the diamict (estimated on the basis of the values in Fig. F24C). Some of the intervals lower in the hole are also potentially subglacial. However, the porosity increase seen at 180 mbsf would not be expected in these lower intervals because the ambient consolidation caused by overburden would already have caused the porosity to reach similar levels to those between 80 and 150 mbsf. Similar porosity level changes in diamicts have been associated with subglacial consolidation at Sites 739 and 742 (Barron, Larsen, et al., 1989). An alternative to shear consolidation would be vertical effective stress imposed by thick ice frozen at its base. However, this would probably have compacted more of the sediment column than just the relatively impermeable diamict. It should be noted, however, that possible overconsolidation by ice overburden was not consistently expressed in the porosities of the materials at Sites 739 and 742 (compare Barron, Larsen, et al., 1989, and Solheim et al., 1991) and could be partly responsible for the porosity variation seen here.

The porosity variation of the sediments may reflect size distribution of clasts and matrix components. However, smear-slide analysis (see

F23. Raw data for NGR, GRAPE density, and magnetic susceptibility, [p. 51](#).



F24. Index properties plots: MAD and GRAPE bulk density, grain density, and porosity, [p. 52](#).



“Site 1097 Smear Slides,” p. 51) suggests the average clay, silt, and biogenic particles of the upper subglacial sequence are 27.1%, 53.3%, and 9.75%, respectively, and the lower subglacial sequence has a similar size distribution (32.0%, 46.6%, and 10.8%). The magnetic susceptibility and natural gamma emission rate of sediments depend upon grain size and mineralogy, and a crossplot of the two subglacial sequences in magnetic susceptibility–NGR space suggests that the two sets of materials belong to the same population (Fig. F25). These similarities strengthen the argument for a subglacial shear origin of porosity changes; if the porosity in the lower subglacial sequence is assumed to represent the normal consolidation porosity for the material composing both sequences, the higher subglacial sequence, which has the same porosity but less overburden, must be overconsolidated. Of course, the lower material may also be overconsolidated, but the porosity step at the base of the upper subglacial sequence cannot be completely the result of the change from poorly to well-sorted material (cf. Site 1103) and must result at least partly from subglacial shear.

Discrete *P*-wave Velocities

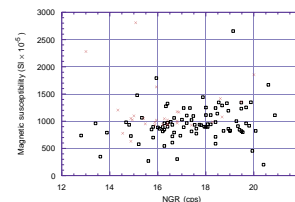
Discrete *P*-wave velocity measurements using the Hamilton Frame sensor pair (PWS3) of the velocity-strength system were made on cores from Hole 1097A for the depth interval 83–400 mbsf (see raw data on CD-ROM and the World Wide Web). Most of the samples were single pieces of matrix-supported diamictite, placed directly (without the liner) between the Hamilton Frame heads. This data set is especially important because the continuity and quality of the recovered cores did not allow any data collection from the MST *P*-wave logging system. The velocity and density (index properties) data correlate very well, indicating good data quality (Fig. F26). The first data point of the velocity diagram is taken from interval velocities derived from seismic reflection profiles crossing the site.

Micromorphology

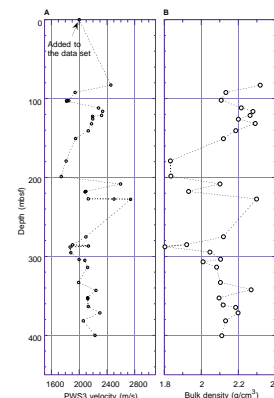
Two samples were taken from Cores 178-1097A-10R and 25R to determine the structural composition of the material by impregnated thin-section analysis. The thin section from Sample 178-1097A-10R-1, 40 cm, shows a diamict with a randomly oriented fabric of sand, silt, and clay particles, through which a mineral showing high birefringence colors was emplaced. This mineral is likely to be calcite, although there is no pervasive calcium carbonate staining in the rest of the slide. The mineral was emplaced in a discrete vein that also shows some shear-zone attributes (clear shear geometry and offset limbs). Pyrite is also clearly present within the vein. Areas of biogenic material and a few areas outside the vein have also undergone precipitation and/or replacement by the two vein minerals. The slide also shows an intra-clast of reworked diamict similar to the groundmass.

The cemented nature of the material may explain the recovery improvement in this core (the material is stiffer), as well as the higher *P*-wave velocity found at ~90 mbsf (see “Seismic Stratigraphy,” p. 18). There is no indication in the seismic profile that the shear noted in association with the mineral deposition was the result of large-scale faulting. The geometry of soft-sediment shear zones is largely pressure controlled (Arch et al., 1988). Glacial sediments of the type seen in Section 178-1097A-10R-1 are usually found to have deformed pervasively,

F25. Magnetic susceptibility vs. natural gamma emission rates of sediments from subglacial intervals, p. 53.



F26. Comparison of PWS3 velocity and MAD bulk density, p. 54.



suggesting low effective pressures that are in line with our knowledge of subglacial environments. Thus, the discrete shear geometry of the mineralized areas (in a material with such a broad and potentially disruptive grain-size range) and the absence of an orientated fabric in the surrounding material (without a pervasive calcium carbonate cement) indicate that the confining pressure at the time of shear was higher than that likely subglacially, or that the material was lithified before subglacial fracture. Both situations would have protected fabrics around the shear from reorientation. Thus, the shearing is unlikely to represent subglacial soft-bedded deformation of the original diamict per se. The ultimate origin of the remaining material may, of course, still involve subglacial deformation. Subglacial shear has been suggested for the interval between 80 and 150 mbsf on the basis on porosity (above), large-scale structure, and the quality of biogenic material (see “**Lithostratigraphy**,” p. 3), which suggests that the highly cemented Core 178-1097A-10R is not a representative sample of the interval that it overlies, which was considerably weaker when brought to atmospheric pressure.

The thin section from Sample 178-1097A-25R-1, 91 cm (Fig. F27), is from a laminated diamict. The laminae are beds of slightly varied grain-size distribution in the fine sand to silt component, which are disrupted, discontinuous, and ~3 mm thick. A pervasive fabric is oriented in the direction of bedding. The fabric gives a strong to moderate extinction to the matrix and probably resulted from shear. Although such a fabric may be produced by deposition from a fluid, particularly after consolidation, the angle of the bedding at 20° from vertical and the pervasively disrupted and discontinuous nature of the beds suggest shear reorientation of the grains. The material also shows some burrowing, the traces of which are sites of pyrite deposition. We could not determine whether the bioturbation occurred before or after the shearing. Given the pervasive nature of the shear fabric, however, it is highly likely that the shear preceded at least the majority of the bioturbation.

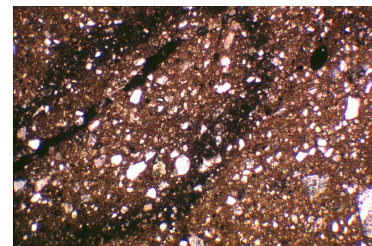
The evidence above indicates the sedimentation of a material of a wide and varying size range. The beds show no internal sorting suggestive of separation through a water column, although negative evidence is not sufficient to rule out this possibility. Sedimentation was followed by deformation and bioturbation. As such, the structural and deformational evidence matches the glaciomarine origin for the material at this depth in the sediment body proposed from macroscopic evidence (see “**Lithostratigraphy**,” p. 3). However, the evidence also encompasses the possibility of deposition into a subglacial water body that has been overridden by a glacier with only a thin or rising deformation layer. Pyrite deposition and shear alignment of the matrix grains at an oblique angle to the drilling direction may explain the relatively good recovery for this length of core.

SEISMIC STRATIGRAPHY

Previous seismic stratigraphic interpretations exist for the vicinity of Site 1097, based on single-channel seismic (Bart and Anderson, 1995) and MCS profiles (Larter and Barker, 1989, 1991b; Larter et al., 1997) (see “**Background and Scientific Objectives**,” p. 1).

The existing multichannel and single-channel seismic profiles across Site 1097, collected by CSIC-Universidad de Granada and Rice University, respectively (Fig. F2; also see “**Appendix**,” p. 24, and Fig. AF1,

F27. Photomicrograph of Sample 178-1097A-25R-1, 91 cm, p. 55.



p. 59, both in the “Leg 178 Summary” chapter, and “Seismic Stratigraphy,” p. 29, in the “Explanatory Notes” chapter), have been re-examined to establish the seismic stratigraphy described below. Individual laboratory (Hamilton Frame) measurements of *P*-wave velocity on cores recovered at Site 1097 have been used to estimate velocities and thus to assign depths to reflectors.

Seismic Units

Acoustic stratigraphy at Site 1097 is characterized by a sequence of reflectors that dip gently seaward from the mid-shelf high (MSH), a structural high located ~27 km landward of Site 1097 (Larter and Barker, 1991b; Barker and Camerlenghi, [Chap. 2](#), this volume). We differentiate three seismic units (Figs. [F28](#), [F29](#)) that coincide with Sequence Groups S1, S2, and S3 of Larter and Barker (1991b) and Larter et al. (1997).

Seismic Unit I (0–80 mbsf)

The upper 30–40 mbsf of seismic Unit I is obscured by the gun reverberation, accentuated in the single-channel seismic profile (see Fig. [F1](#)). The lower part of Unit I at the site location is characterized by nearly flat-lying moderate- to low-amplitude discontinuous reflectors, which change toward the shelf edge to low-angle dipping reflectors of weak amplitude. Landward, these reflectors pinch out ~20 km from Site 1097 before reaching the MSH. The lower boundary of seismic Unit I is marked by a high-amplitude reflector that farther offshore truncates reflectors from the underlying seismic Unit II.

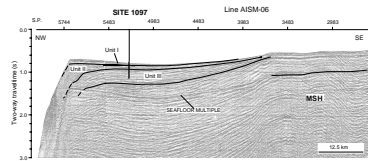
Seismic Unit II (80–150 mbsf)

Seismic Unit II has a wedge geometry. At Site 1097, it is characterized by gently dipping high- to moderate-amplitude semicontinuous topset reflectors. The varied acoustic character of Unit II is best explained by variable *P*-wave velocities and bulk densities from sediments cored at Site 1097 (i.e., 2450 m/s at the top and 1950 m/s toward the bottom) (Fig. [F30](#)). Thickness of seismic Unit II increases toward the outer shelf, where gently dipping topset reflectors grade into weak amplitude, steeply dipping foresets. Seismic Unit II thins gradually landward until it pinches out at the MSH. The lower boundary of Unit II is a high-amplitude reflector against which outer shelf reflectors from Unit II appear to downlap seaward of Site 1097, indicating a prograding sequence.

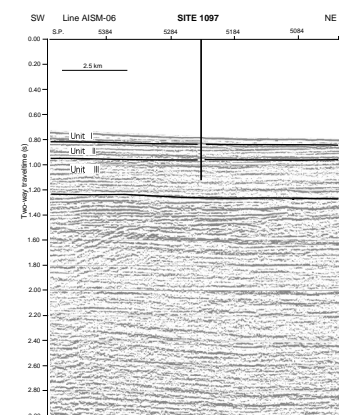
Seismic Unit III (150–410 mbsf)

Seismic Unit III (150–410 mbsf and continuing to beneath the cored section) is marked by gently dipping reflectors that become more steeply dipping toward the outer shelf. The seaward vertical stacking of reflectors indicates an aggrading to moderately prograding sequence. Reflectors from seismic Unit III are characterized by lateral changes in amplitude and continuity. Alterations in acoustic character can be explained by variable *P*-wave velocities and bulk densities from sediments cored at Site 1097 (Fig. [F30](#)). The upper 50 m of seismic Unit III has low velocities averaging 1900 m/s. From 200 to 230 mbsf the velocities range from 2100 to 2700 m/s. Below this high-velocity zone, the velocity drops to ~1900 m/s and then slowly increases downhole to

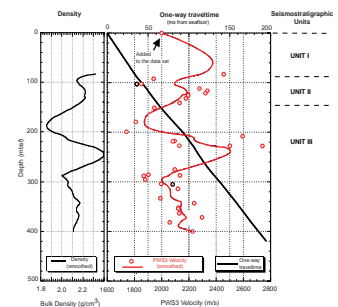
F28. MCS profile AISM-06 across Site 1097, [p. 56](#).



F29. Detail of MCS profile AISM-06 across Site 1097, [p. 57](#).



F30. Traveltime-depth function and correlation between physical properties and seismic units, [p. 58](#).



~2100 m/s at 350 mbsf. Thickness of seismic Unit III decreases gradually landward until it pinches out at the MSH and increases seaward toward the paleoslope. At Site 1097, the Unit III/Unit II boundary (the S3/S2 boundary) appears conformable.

Interpretation

All the seismic units drilled at Site 1097 are the result of glacial sedimentation on the Antarctic Peninsula continental shelf. Although no sediments were recovered from seismic Unit I, the truncation of reflectors from the underlying unit suggests erosion at its base, possibly by ice-sheet advance. Sediments recovered from seismic Unit II (80 to 150 mbsf) are characterized by massive diamicts that are interpreted as deforming tills (see “[Lithostratigraphy](#),” p. 3). This lithologic interpretation is compatible with biostratigraphic, reworked assemblages that indicate subglacial till deposition (Zone I; see “[Biostratigraphy](#),” p. 8). These sediments suggest that during the development of seismic Unit II, a grounded ice sheet regularly extended at least to where Site 1097 is located and probably to the shelf edge. These results confirm the interpretations of Larter and Barker (1989, 1991) and Larter et al. (1997).

In the upper part of seismic Unit III (198–235 mbsf), core recovery improved. This coincides with a change downhole to lower *P*-wave velocities and moderate amplitude reflectors, a lithologic change from the massive diamict of Unit II to muddy diamict (see “[Lithostratigraphy](#),” p. 3), and the beginning of biostratigraphic Zone II (see “[Biostratigraphy](#),” p. 8), all of which indicate an ice-proximal marine environment.

Drilling results from Site 1097 show that all three seismic units were deposited under a glacial regime and differentiate two stages of margin growth. During the time of deposition of seismic Unit III, margin growth was characterized by vertical aggradation to moderate progradation of the continental margin (Fig. [F28](#)). During deposition of seismic Units I and II, glacial sequences show more pronounced progradation (3 km), expressed by low-angle topsets and steep foresets (Fig. [F28](#)). The differences between seismic Units II and III in the stacking patterns of glacial sequences seaward of the drill site suggest an important change in the style of sedimentation, linked to a change in the glacial regime in this part of the Antarctic margin.

REFERENCES

- Alley, R.B., Blankenship, D.D., Rooney, S.T., and Bentley, C.R., 1989. Sedimentation beneath ice shelves: the view from Ice Stream B. *Mar. Geol.*, 85:101–120.
- Arch, J., Maltman, A.J., and Knipe, R.J., 1988. Shear-zone geometries in experimentally deformed clays: the influence of water content, strain rate and primary fabric. *J. Struct. Geol.*, 10:91–99.
- Barker, P.F., 1995. The proximal marine sediment record of Antarctic climate since the late Miocene. In Cooper, A.K., Barker, P.F., and Brancolini, G. (Eds.), *Geology and Seismic Stratigraphy of the Antarctic Margin*. Am. Geophys. Union, Antarct. Res. Ser., 68:25–57.
- Barron, J., Larsen, B., et al., 1989. *Proc. ODP, Init. Repts.*, 119: College Station, TX (Ocean Drilling Program).
- Bart, P.J., and Anderson, J.B., 1995. Seismic record of glacial events affecting the Pacific margin of the northwestern Antarctic Peninsula. In Cooper, A.K., Barker, P.F., and Brancolini, G. (Eds.), *Geology and Seismic Stratigraphy of the Antarctic Margin*. Antarct. Res. Ser., 68:75–96.
- Boulton, G.S., 1990. Sedimentary and sea level changes during glacial cycles and their control on glaciomarine facies architecture. In Dowdeswell, J.A., and Scourse, J.D. (Eds.), *Glaciomarine environments: processes and sediments*. Geol. Soc. Spec. Publ., 53:15–52.
- Boulton, G.S., 1996. Theory of glacial erosion and deposition as consequence of subglacial sediment deformation. *J. Glaciol.*, 42:43–62.
- Boulton, G.S., and Hindmarsh, R.C.A., 1987. Sediment deformation below glaciers: rheology and geological consequences. *J. Geophys. Res.*, 92:9059–9082.
- Boyce, J.I., and Eyles, N., 1991. Drumlins carved by deforming till streams below the Laurentide Ice Sheet. *Geology*, 19:787–90.
- Clark, P.U., Licciardi, J.M., MacAyeal, D.R., and Jenson, J.W., 1996. Numerical modeling of a soft-bedded Laurentide Ice Sheet during the last glacial maximum. *Geology*, 24:679–682.
- Domack, E.W., 1990. Laminated terrigenous sediments from the Antarctic Peninsula: the role of subglacial and marine processes. In Dowdeswell, J.A., and Scourse, J.D. (Eds.), *Glaciomarine Environments: Processes and Sediments*. Geol. Soc. Spec. Publ. London, 53:91–103.
- Griffith, T.W., and Anderson, J.B., 1989. Climatic controls of sedimentation in bays and fjords of the northern Antarctic Peninsula. *Mar. Geol.*, 85:181–204.
- Hayes, D.E., Frakes, L.A., et al., 1975. *Init. Repts. DSDP*, 28: Washington (U.S. Govt. Printing Office).
- Ishman, S.E., and Webb, P.-N., 1988. Late Neogene benthic foraminifera from the Victoria land basin margin, Antarctica: application to glacio-eustatic and tectonic events. *Rev. Paleontol., Spec. Publ.* 2:523–551.
- Kastner, M., Keene, J.B., and Gieskes, J.M., 1977. Diagenesis of siliceous oozes, I. Chemical controls on the rate of opal-A to opal-CT transformation—an experimental study. *Geochim. Cosmochim. Acta*, 41:1041–1059.
- Krebs, W.N., 1977. Ecology and preservation of neritic marine diatoms, Arthur Harbor, Antarctica [Ph.D. dissert.]. Univ. California, Davis.
- Larter, R.D., and Barker, P.F., 1989. Seismic stratigraphy of the Antarctic Peninsula Pacific margin: a record of Pliocene–Pleistocene ice volume and paleoclimate. *Geology*, 17:731–734.
- Larter, R.D., and Barker, P.F., 1991a. Effects of ridge-crest trench interaction on Antarctic-Phoenix spreading: forces on a young subducting plate. *J. Geophys. Res.*, 96:19583–19607.
- Larter, R.D., and Barker, P.F., 1991b. Neogene interaction of tectonic and glacial processes at the Pacific margin of the Antarctic Peninsula. In Macdonald, D.I.M. (Ed.),

- Sedimentation, Tectonics and Eustasy: Sea-level Changes at Active Margins*. Spec. Publ. Int. Assoc. Sedimentol., 12:165–186.
- Larter, R.D., Rebesco, M., Vanneste, L.E., Gamboa, L.A.P., and Barker, P.F., 1994. Seismic reflection investigations on the Pacific margin of the Antarctic Peninsula. *Terra Antarct.*, 1:271–274.
- Larter, R.D., Rebesco, M., Vanneste, L.E., Gamboa, L.A.P., and Barker, P.F., 1997. Cenozoic tectonic, sedimentary and glacial history of the continental shelf west of Graham Land, Antarctic Peninsula. In Barker, P.F., and Cooper, A.K. (Eds.), *Geology and Seismic Stratigraphy of the Antarctic Margin* (Pt. 2). Antarct. Res. Ser., 71:1–27.
- Osterman, L.E., 1984. Benthic foraminiferal zonation of a glacial-interglacial transition from Frobisher Bay, Baffin Island, N.W.T., Canada. In Oertli, H.J. (Ed.), *Benthos '83*, 471–476.
- Pope, P.G., and Anderson, J.B., 1992. Late Quaternary glacial history of the northern Antarctic Peninsula's western continental shelf: evidence from the marine record. In Elliot, D. H. (Ed.), *Contributions to Antarctic Research III*. Am. Geophys. Union, Antarct. Res. Ser., 57:63–91.
- Pudsey, C.J., Barker, P.F., and Larter, R.D., 1994. Ice sheet retreat from the Antarctic Peninsula shelf. *Cont. Shelf Res.*, 14:1647–1675.
- Rebesco, M., Camerlenghi, A., and Zanolla, C., in press. Bathymetry and morphogenesis of the continental margin west of the Antarctic Peninsula. *Terra Antarct.*
- Solheim, A., Forsberg, C.F., and Pittenger, A., 1991. Geotechnical properties of glacial shelf sediments from Prydz Bay, East Antarctica. In Barron, J., Larsen, B., et al., *Proc. ODP, Sci. Results*, 119: College Station, TX (Ocean Drilling Program), 143–167.
- Vanneste, L.E., and Larter, R.D., 1995. Deep-tow boomer survey on the Antarctic Peninsula Pacific margin: an investigation of the morphology and acoustic characteristics of Late Quaternary sedimentary deposits on the outer continental shelf and upper slope. In Cooper, A.K., Barker, P.F., and Brancolini, G. (Eds.), *Geology and Seismic Stratigraphy of the Antarctic Margin*. Am. Geophys. Union, Antarct. Res. Ser., 68:97–121.
- Walker, R.G., 1992. Turbidites and submarine fans. In Walker, R.G., and James, N. (Eds.), *Facies Models: Response to Sea Level Change*: St. Johns, Newfoundland (Geol. Assoc. Canada), 239–264.
- Webb, P.-N., 1974. Micropaleontology, paleoecology and correlation of the Pecten Gravels, Wright Valley Antarctica and the description of *Trochoelphidiella onyxi*, n. gen., n. sp. *J. Foraminiferal Res.*, 4:184–199.

Figure F1. Location of Site 1097 on single-channel seismic reflection profile PD88-04 (Bart and Anderson, 1995) across the continental shelf seaward of Adelaide Island, Antarctic Peninsula.

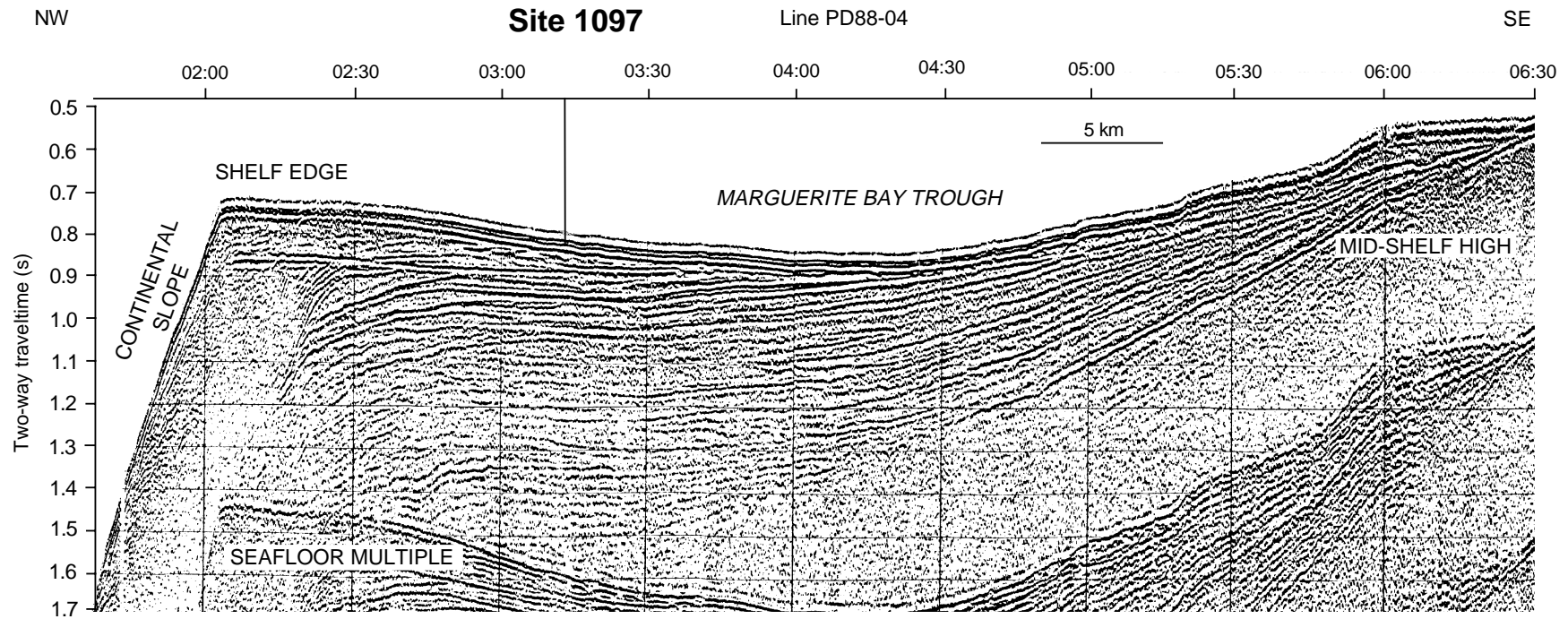


Figure F2. A. Bathymetric map (after Rebesco et al., in press) and main morphologic elements of the continental shelf across Marguerite Bay Trough (Pope and Anderson, 1992) and Lobes 3 and 4 (Larter et al., 1994, 1997). (Continued on next page.)

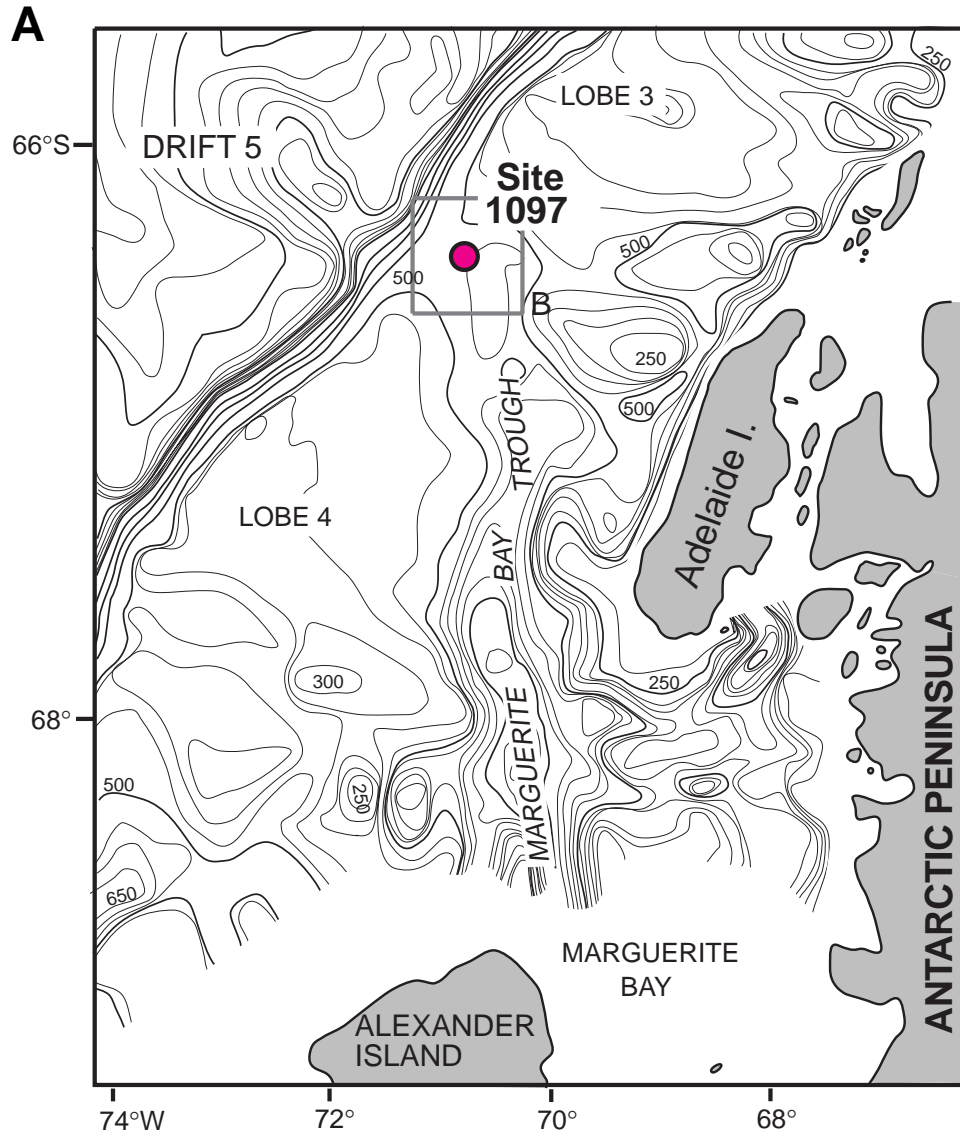


Figure F2 (continued). B. Multichannel and single-channel seismic reflection profiles (thin lines) on and around Site 1097 (for line identification, see "Seismic Stratigraphy," p. 29, in the "Explanatory Notes" chapter). The 3.5-kHz profiles acquired during approach and on transit toward Site 1098 are indicated by bold lines.

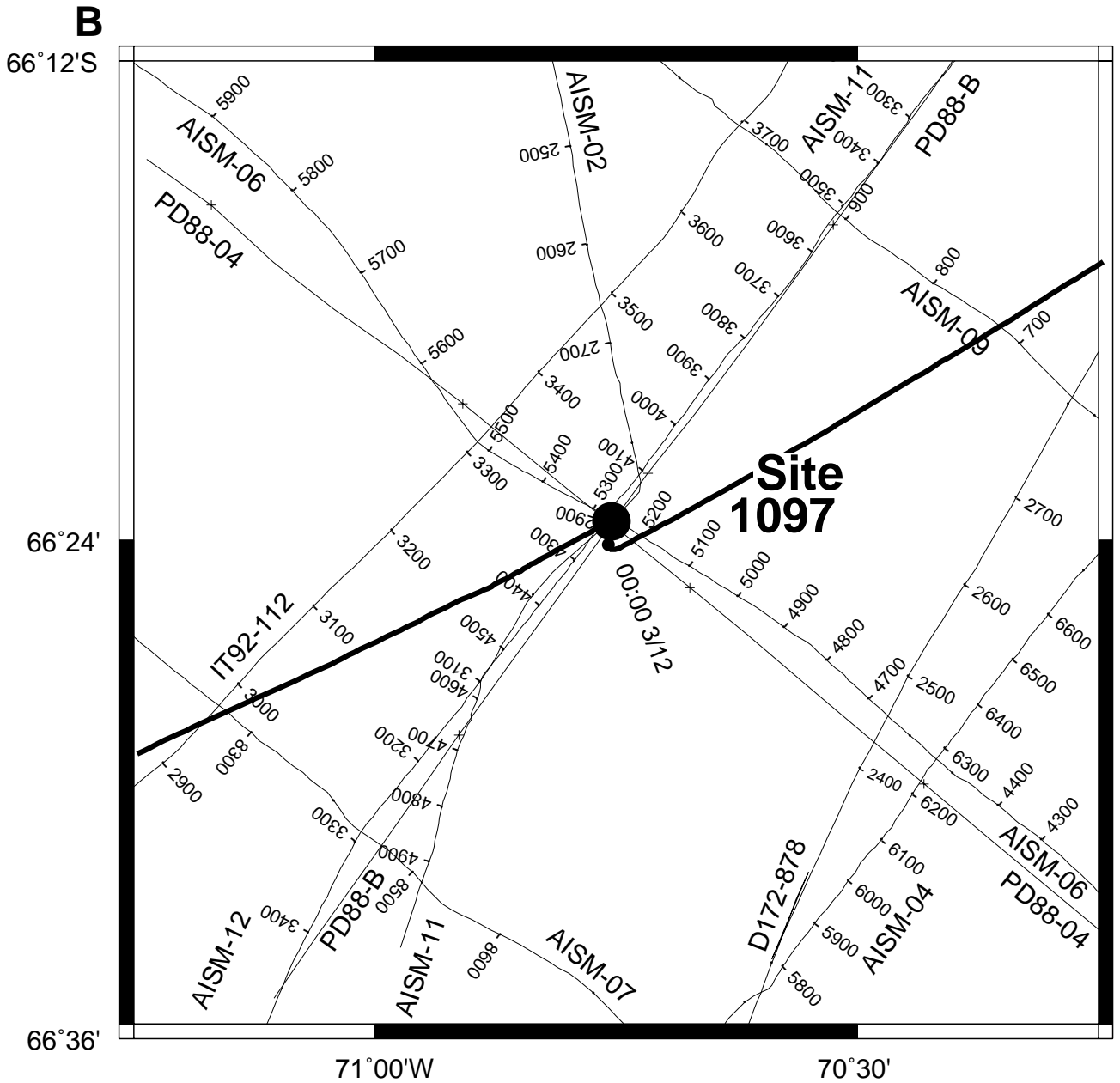


Figure F3. The 3.5-kHz sub-bottom profile across Site 1097, acquired during site approach (see Fig. F2B, p. 25). The site is located within a broad trough, and seafloor morphology may reflect iceberg scour.

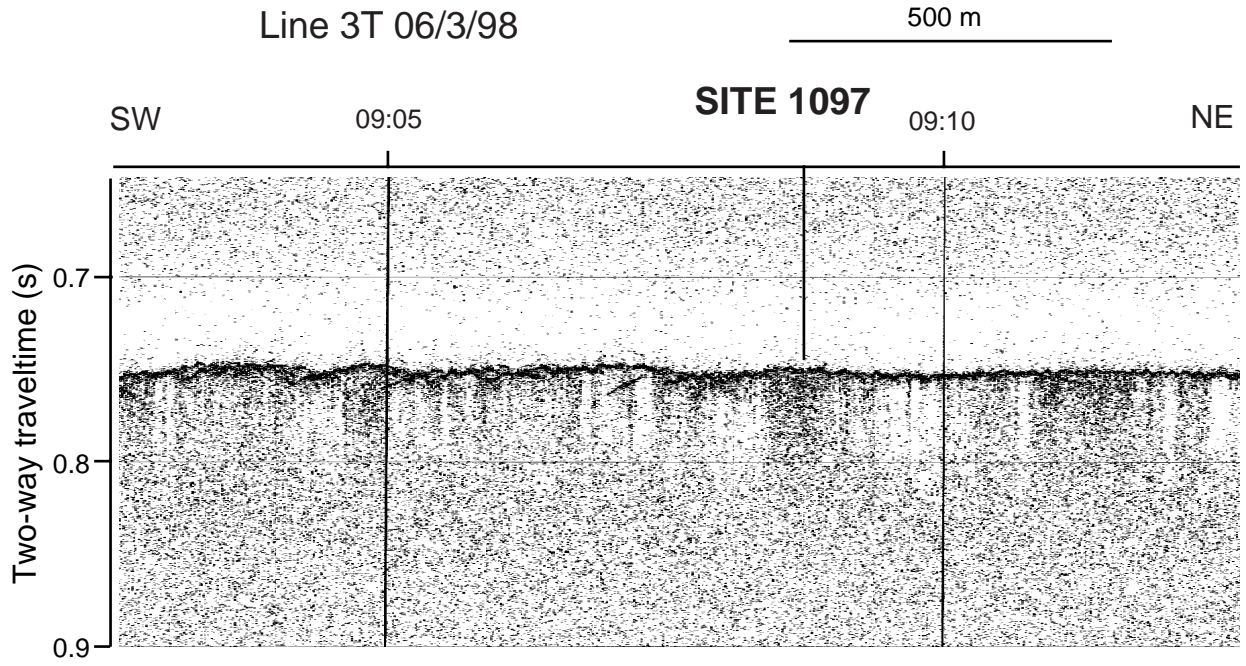


Figure F4. Icebergs were targeted and tracked over a 24-mi range with the two bridge radars. The track of one iceberg at Site 1097 is shown. This iceberg forced us to pull out of the free-fall funnel and halt coring operations in Hole 1097A. While on site throughout the leg, a total of 74 icebergs were tracked, most of them at Palmer Deep (Sites 1098 and 1099). Data compiled by Andy Caldwell, Leg 178 ice observer.

Iceberg #43 at Site 1097
2000 hr 6 March 1998 to
1400 hr 9 March 1998

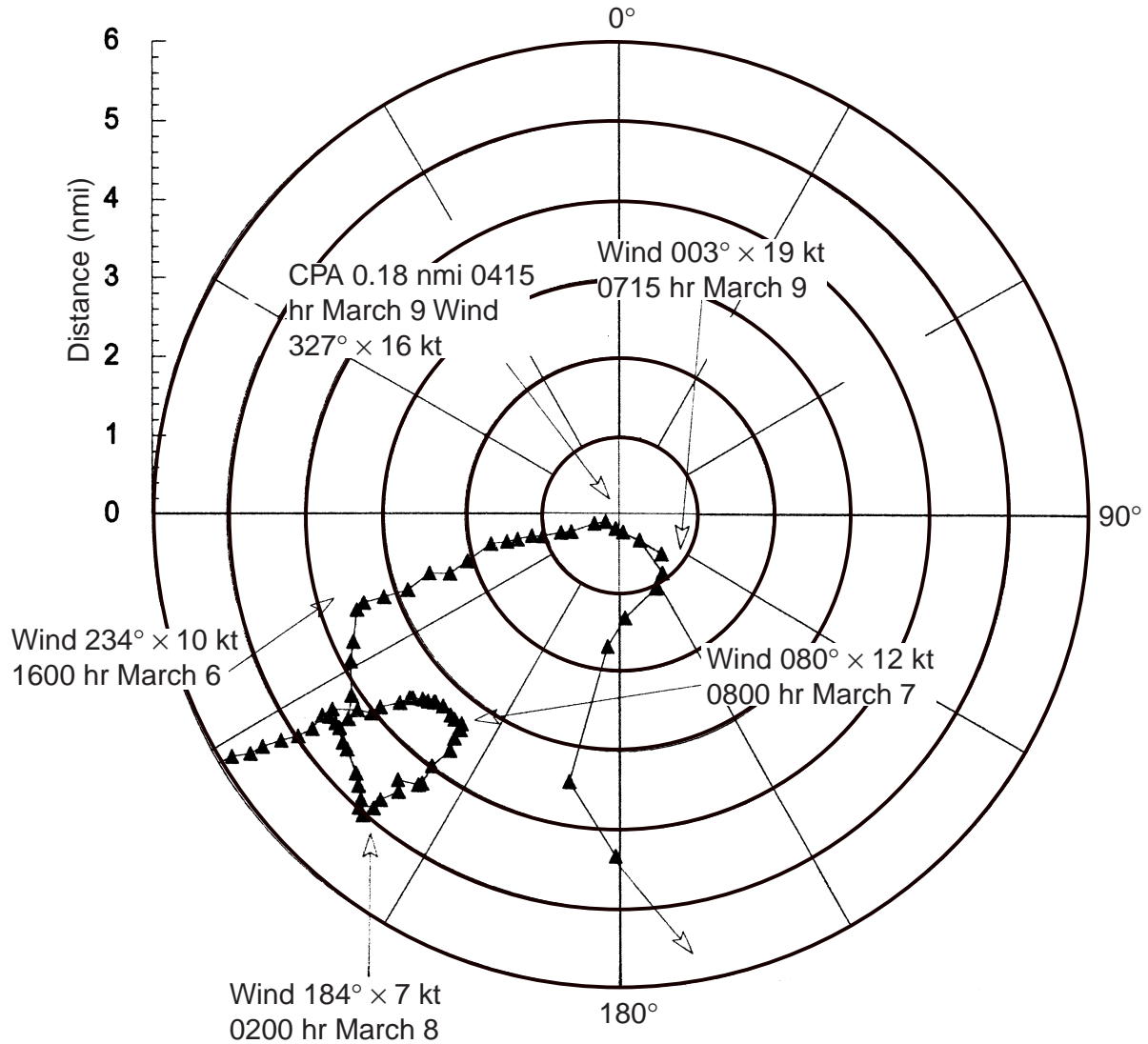


Figure F5. Lithofacies, biofacies, age, and inferred environmental setting for Hole 1097A.

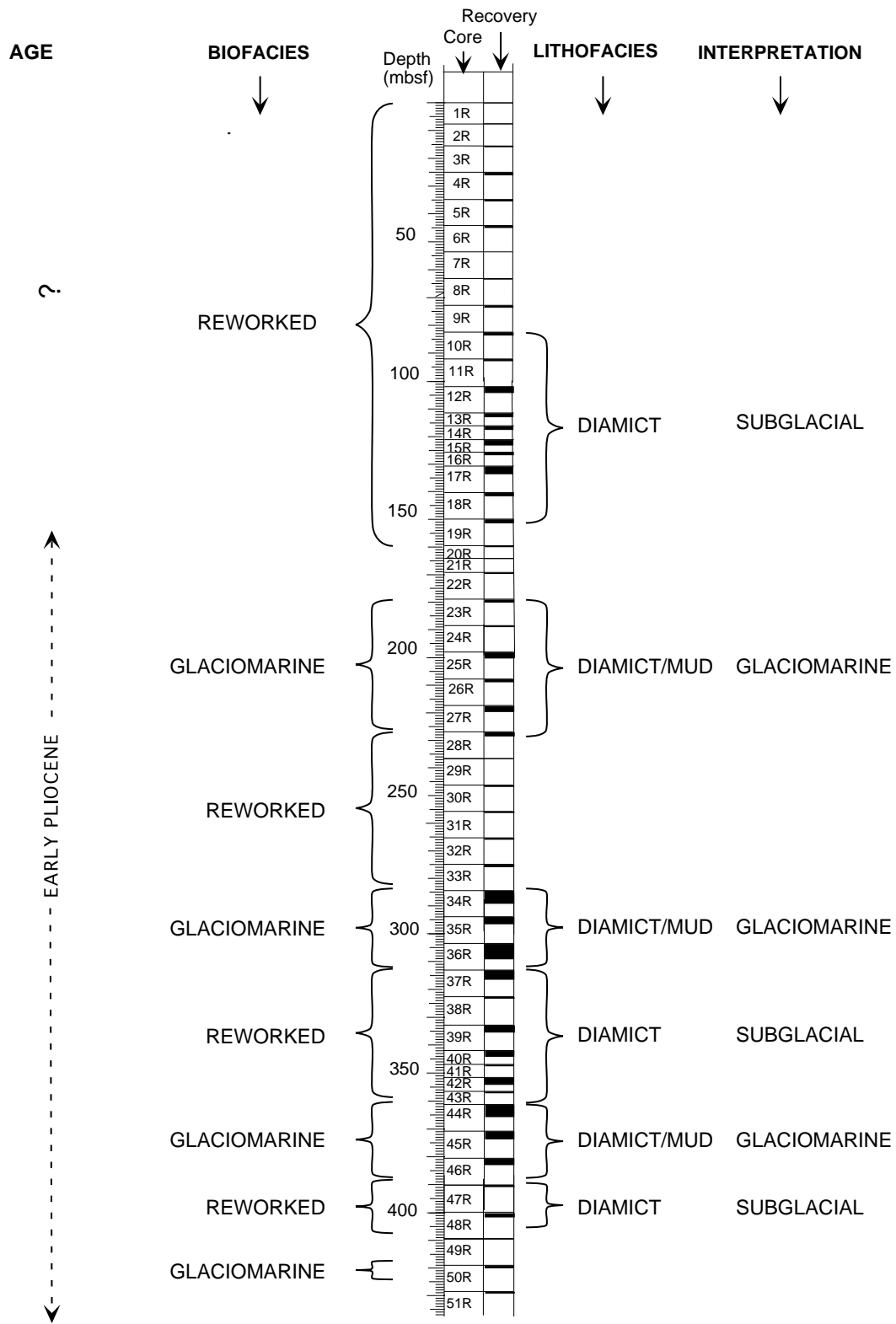


Figure F6 (continued).

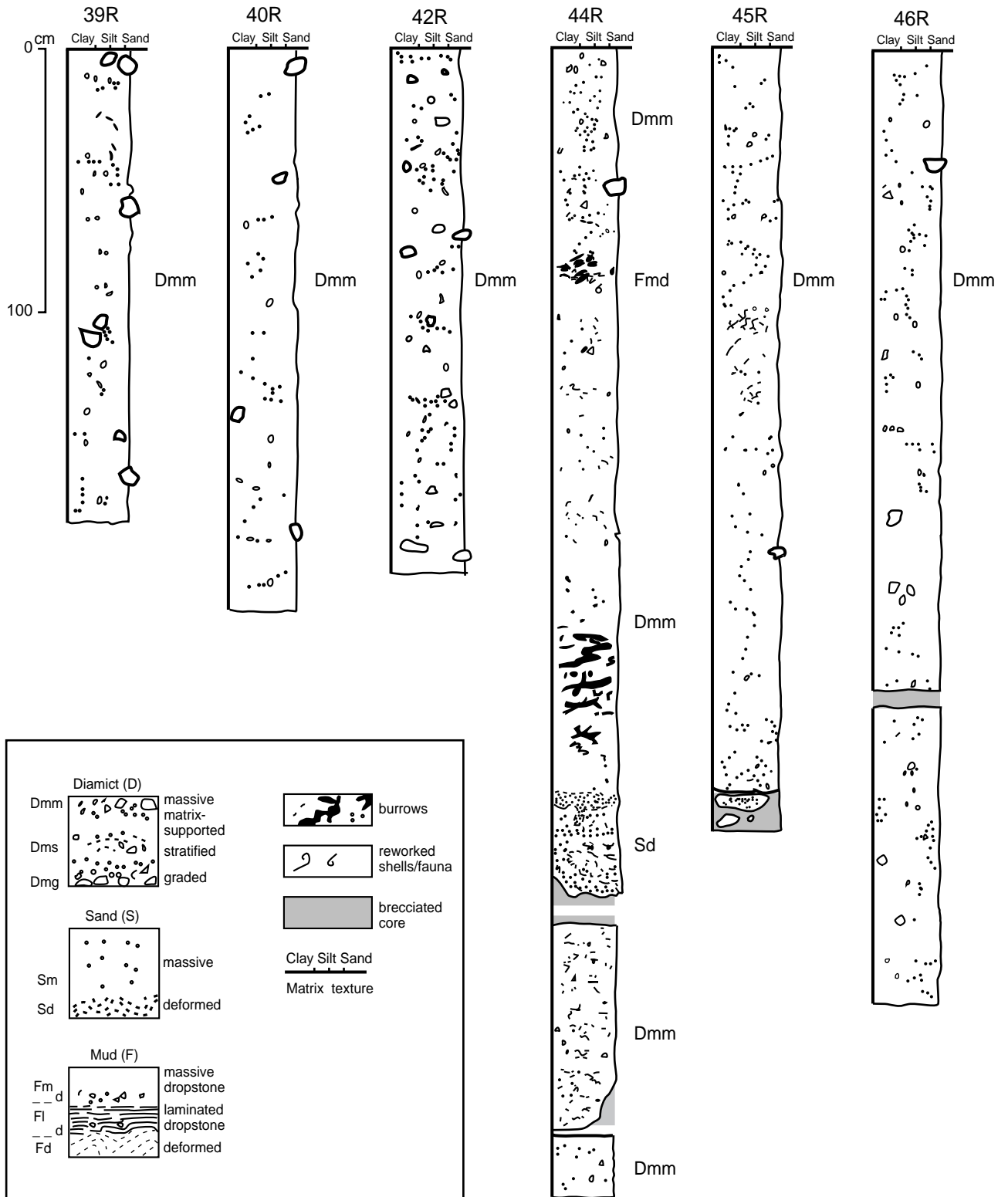


Figure F7. Representative examples of massive diamict lithofacies from Site 1097. A. Interval 178-1097A-10R-1, 38–49 cm. B. Interval 178-1097A-12R-1, 95–110 cm. (Continued on next three pages.)

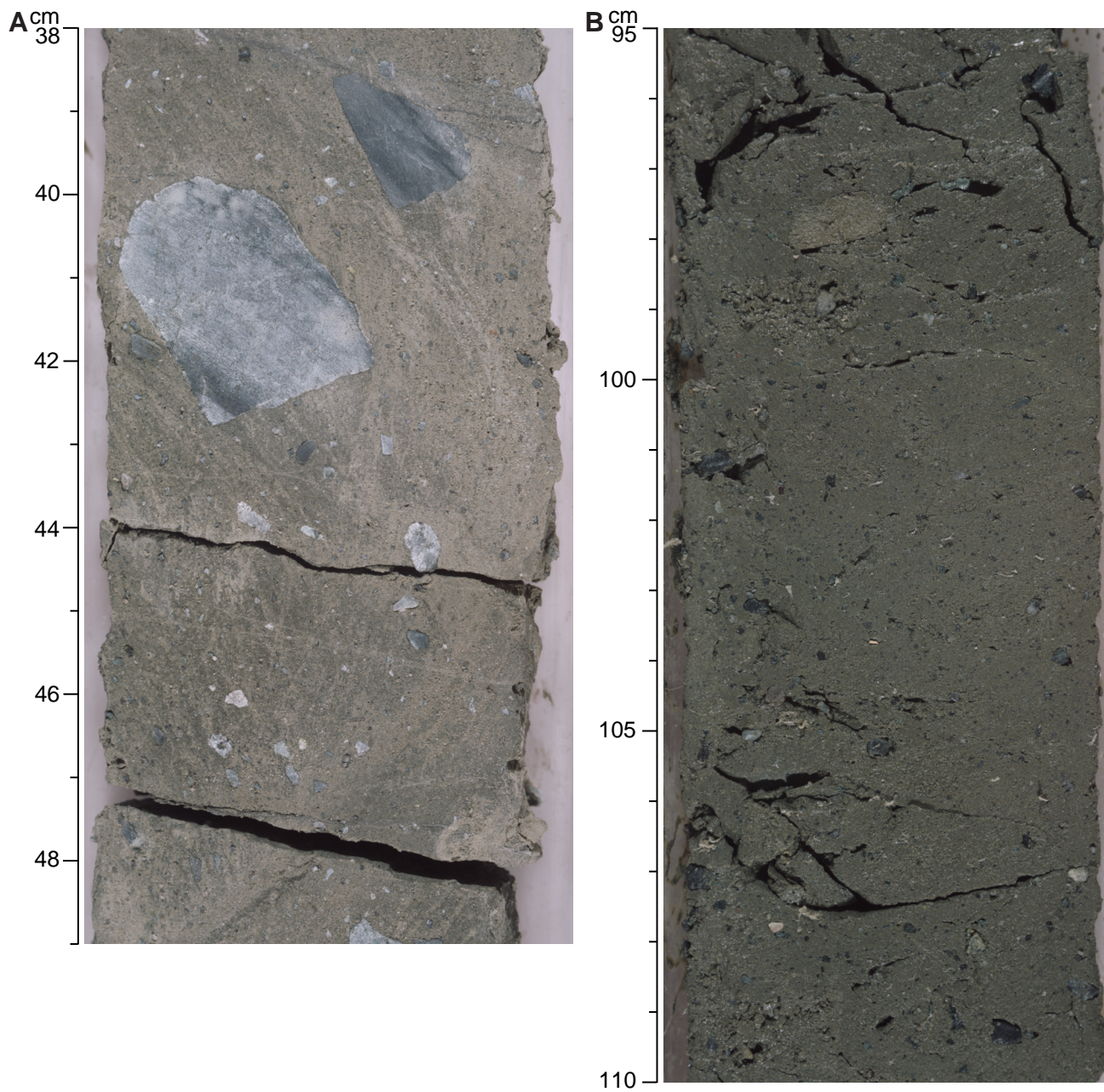


Figure F7 (continued). C. Interval 178-1097A-13R-1, 78–89 cm.

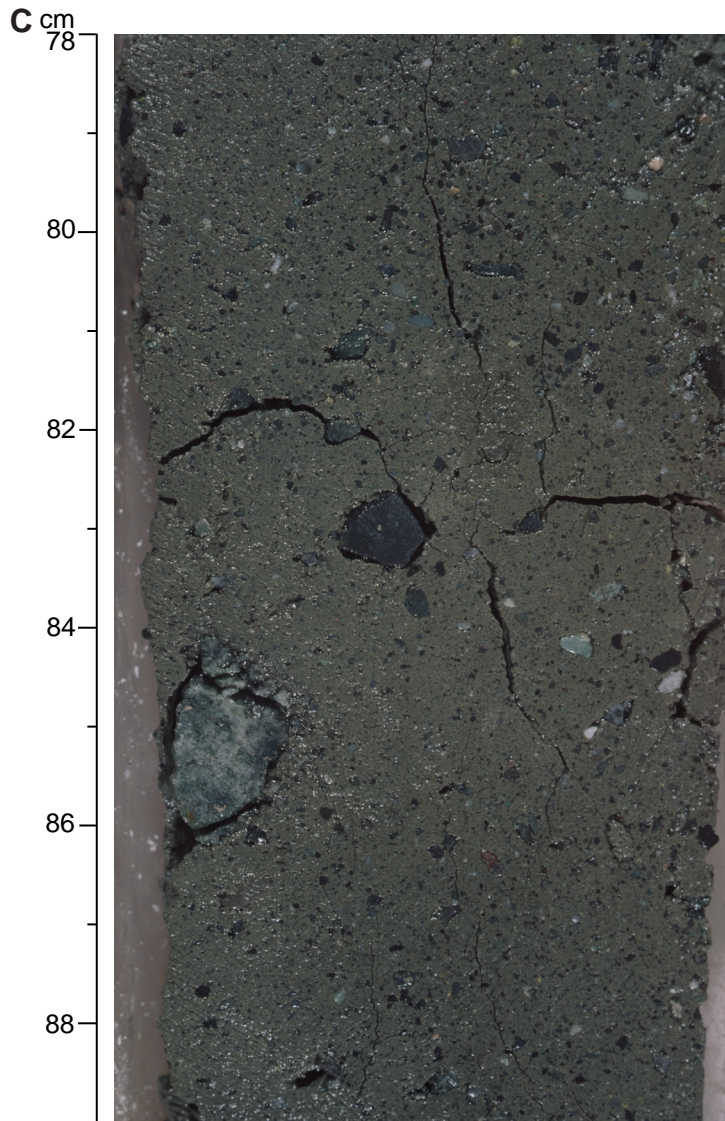


Figure F7 (continued). D. Interval 178-1097A-45R-2, 108–117 cm.

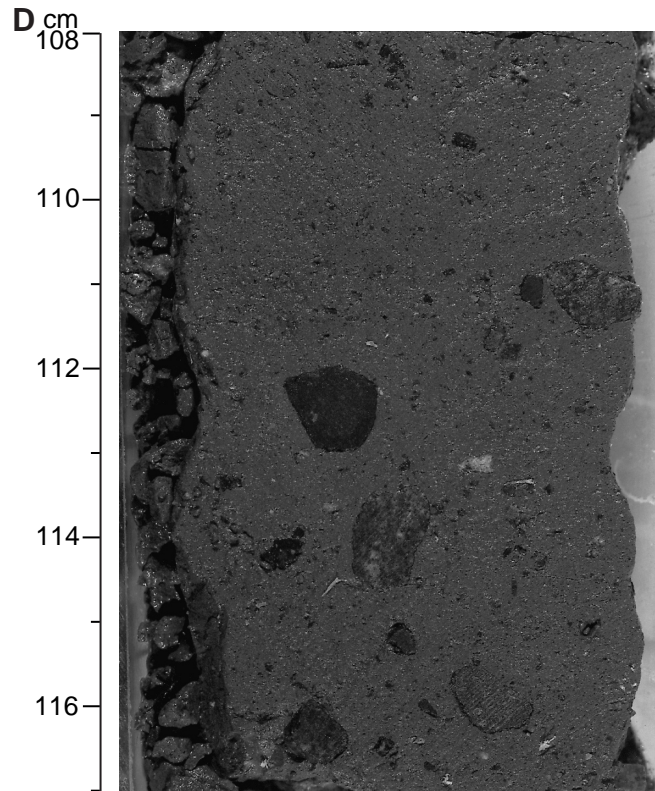


Figure F7 (continued). E. Massive diamict facies showing marked fissility created by very thin (millimeter) silt laminae (interval 178-1097A-16R-1, 0-30 cm).

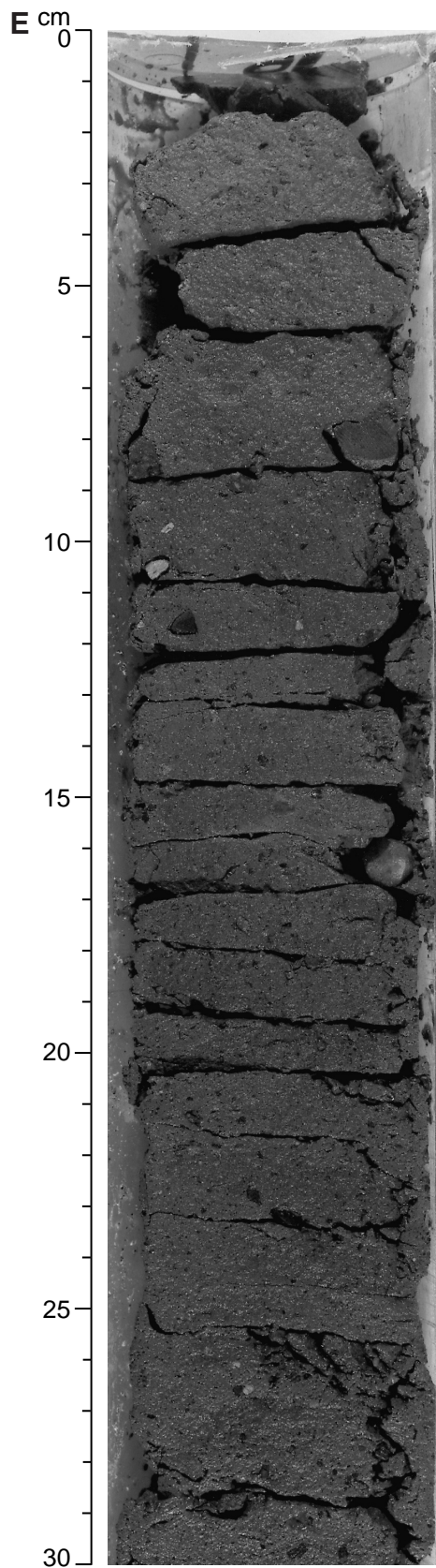


Figure F8. Distribution of dip angles of elongate clasts in massive diamict having a long axis >0.5 mm, Hole 1097A.

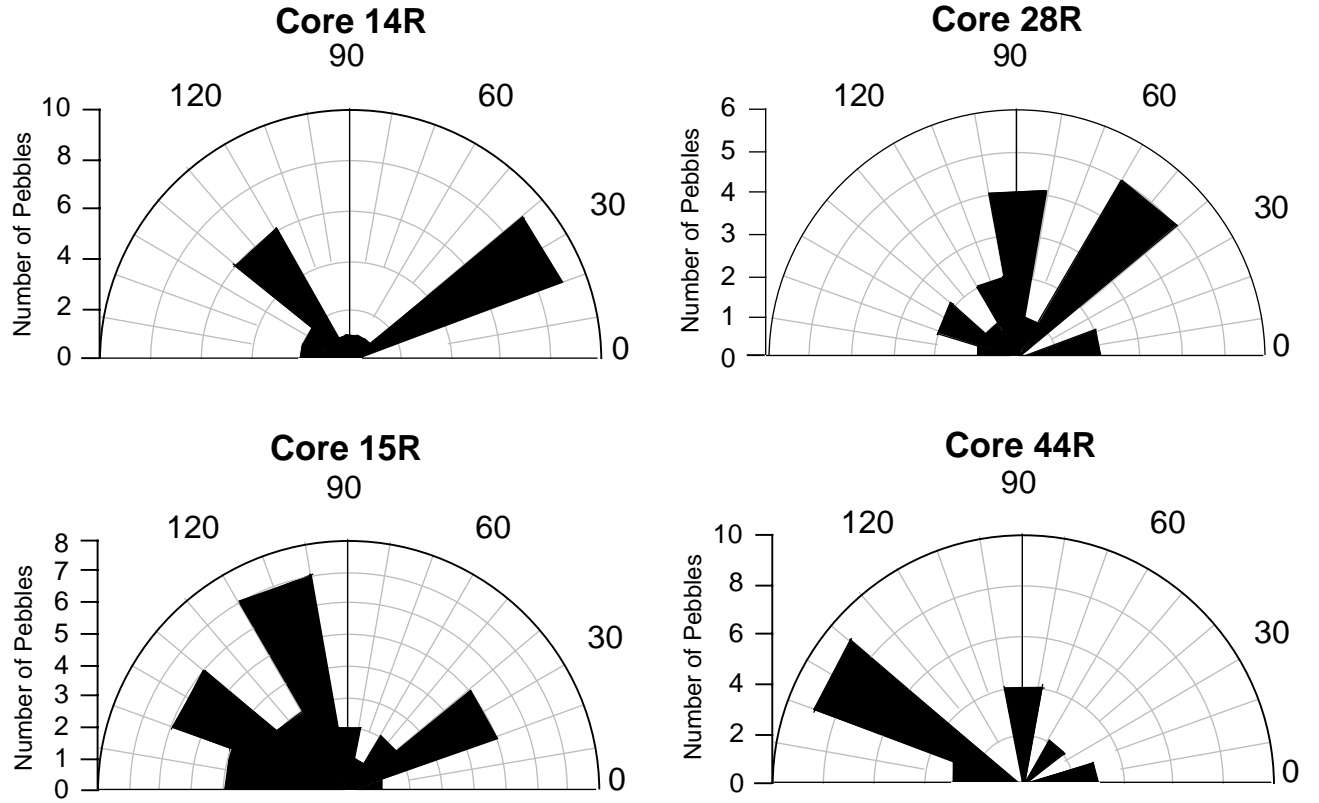


Figure F9. Downhole clast lithology from Site 1097.

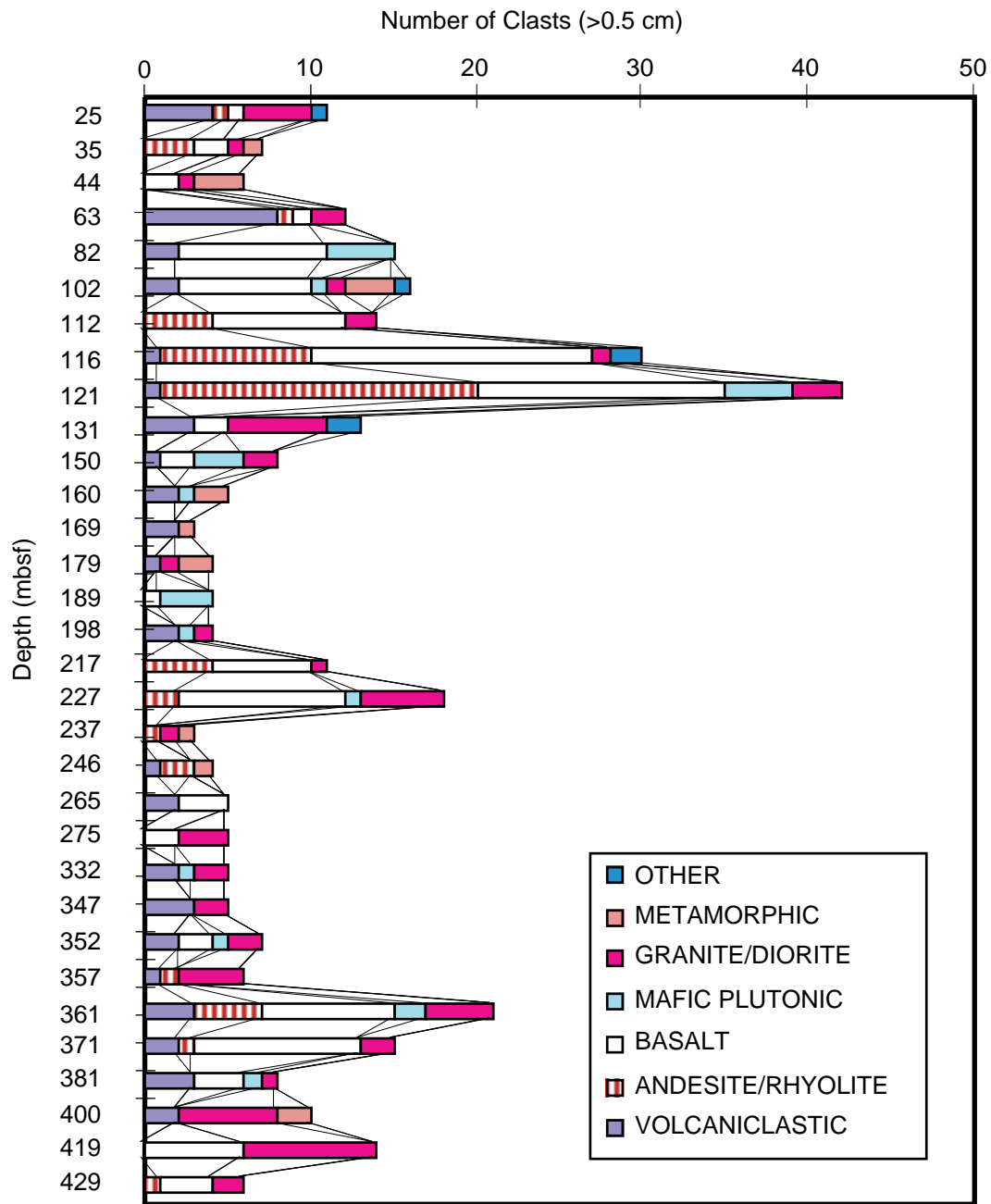


Figure F10. Graded diamict facies at Hole 1097A. A. Interval 178-1097A-27R-1, 108–120 cm, showing top of normally graded diamict with overlying laminated marine muds. B. Top of normally graded diamict facies in interval 178-1097A-27R-1, 37–62 cm; the large rounded clast at 56 cm is a rip-up clast of altered tephra. (Continued on next page.)

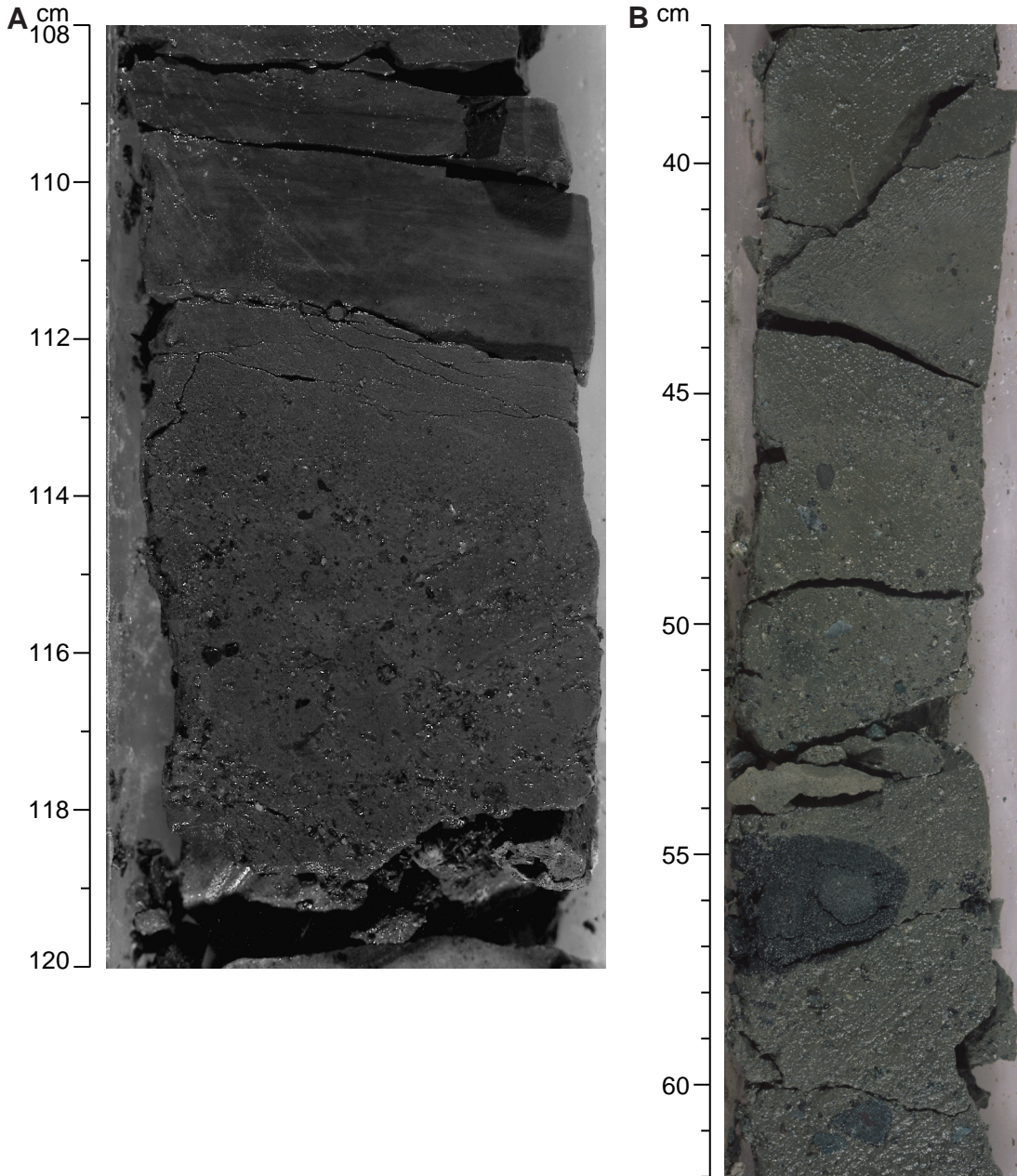


Figure F10 (continued). C. Bioturbated marine muds separating graded diamict beds in interval 178-1097A-27R-1, 87-102 cm. For graphic log, see Figure F6, p. 29.

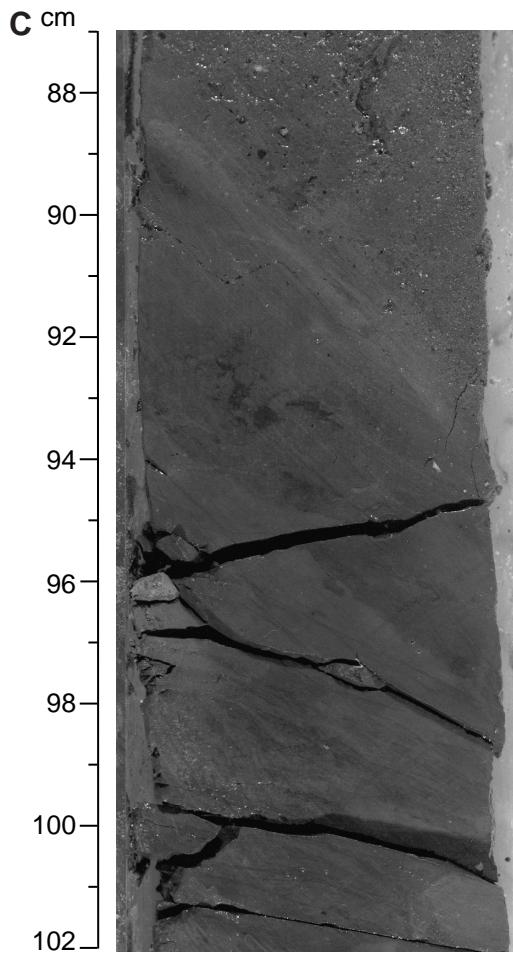


Figure F11. Stratified diamict facies from Hole 1097A. A. Stratified diamict facies composed of alternating clast-rich and clast-poor silty clay (interval 178-1097A-25R-1, 19–46 cm). B. Interval 178-1097A-25R-1, 87–97 cm, showing alternation of clast-poor and clast-rich diamict. For graphic log, see Figure F6, p. 29.

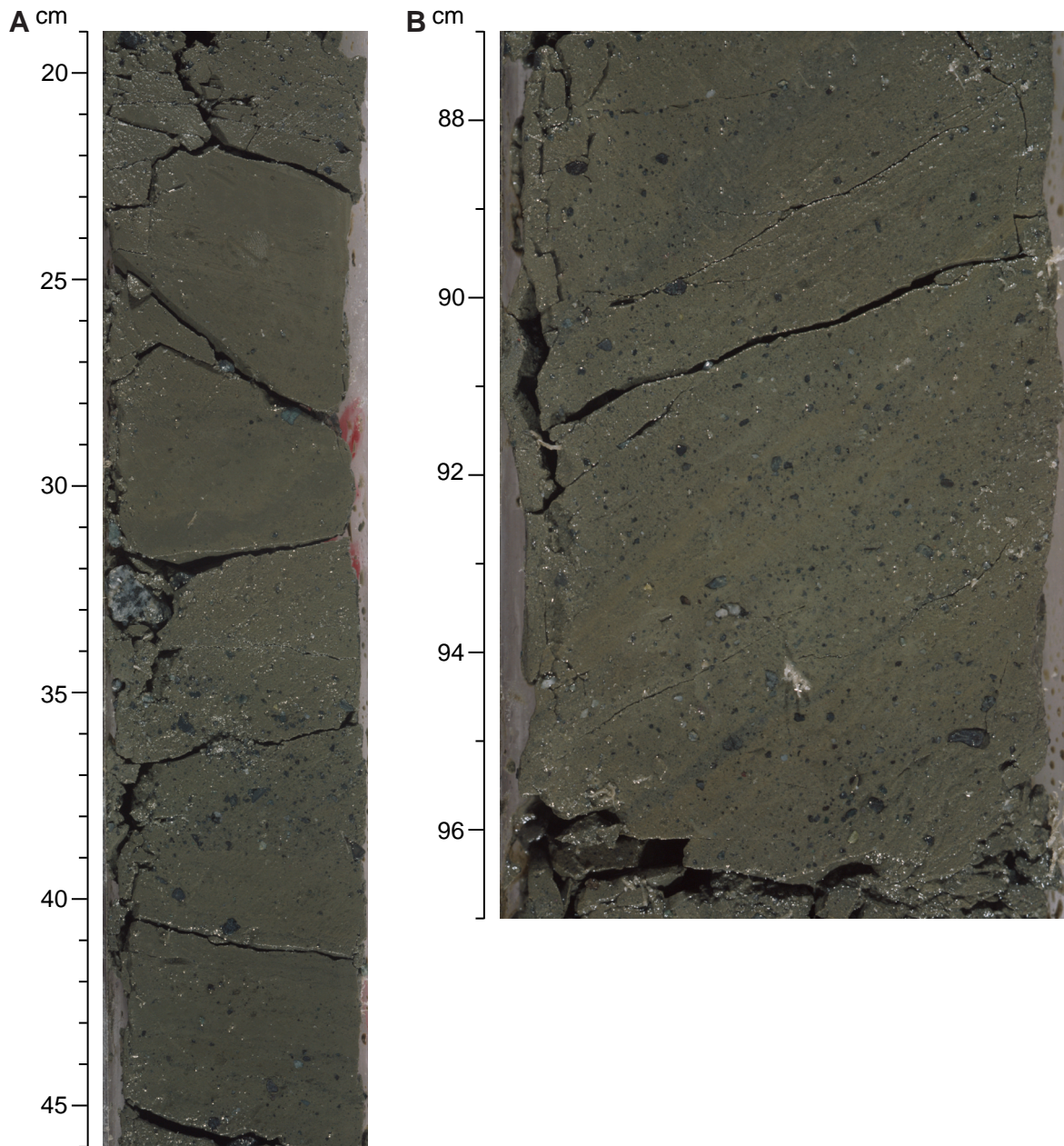


Figure F12. Weakly laminated silty clay with ice-rafted clasts (interval 178-1097A-34R-1, 26–40 cm). This facies is transitional to diamict (Fig. F6, p. 29).

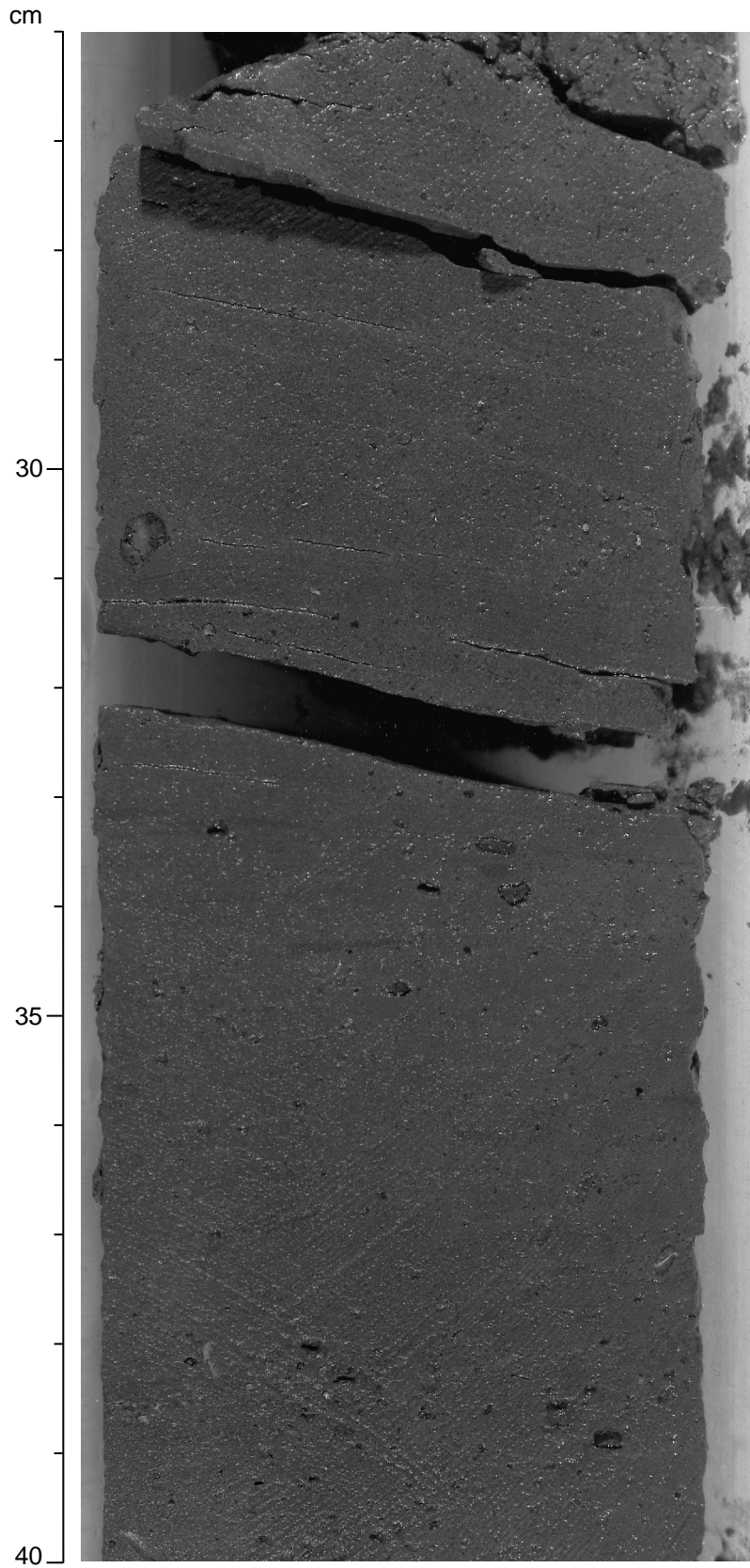


Figure F13. Summary of facies recovered at Site 1097, associated biofacies, and environmental interpretation. Representative cores are identified at the top.

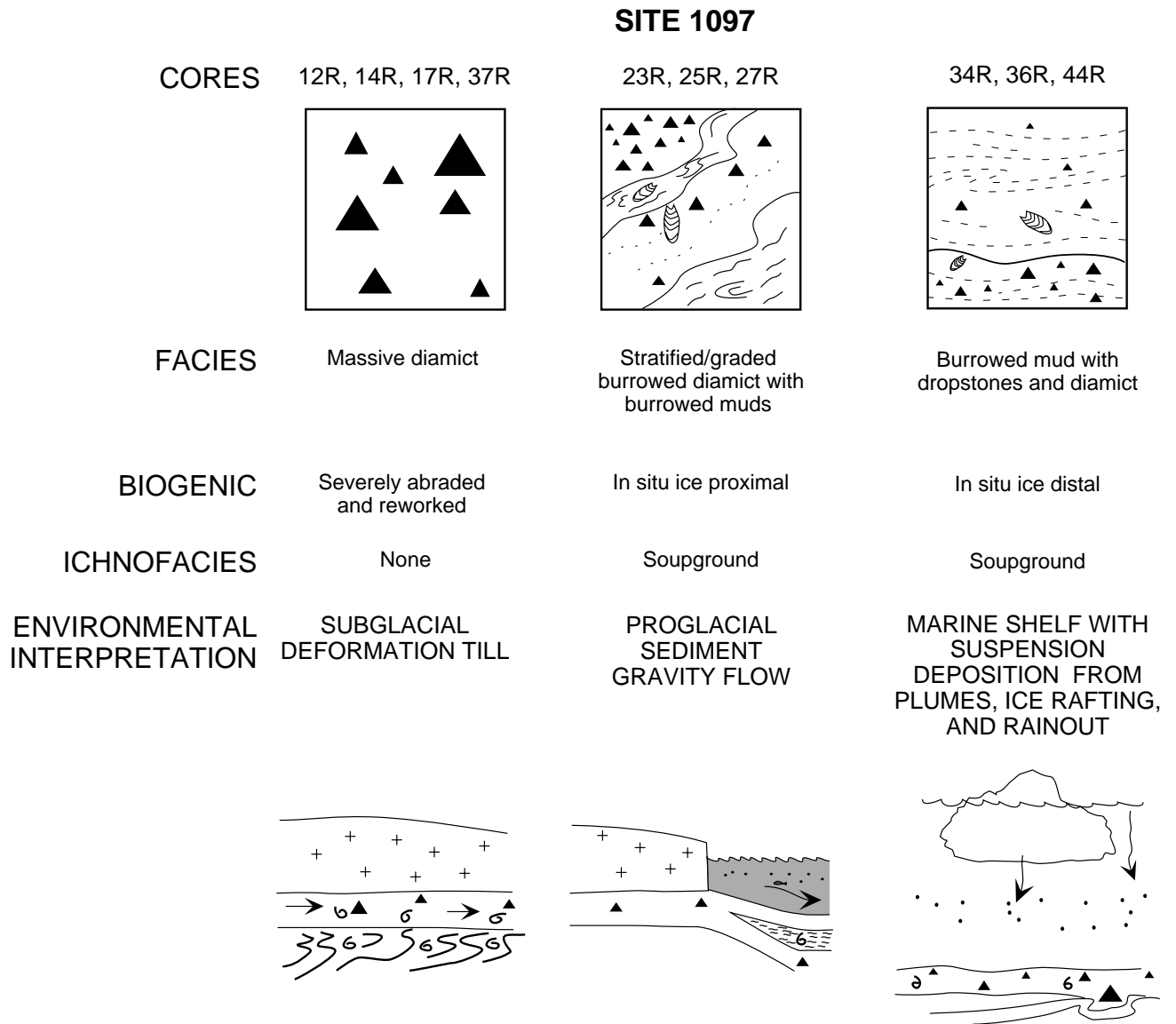


Figure F14. A summary of the occurrence of diatoms, radiolarians, and planktonic foraminifers at Site 1097. Stippled intervals = barren of microfossils.

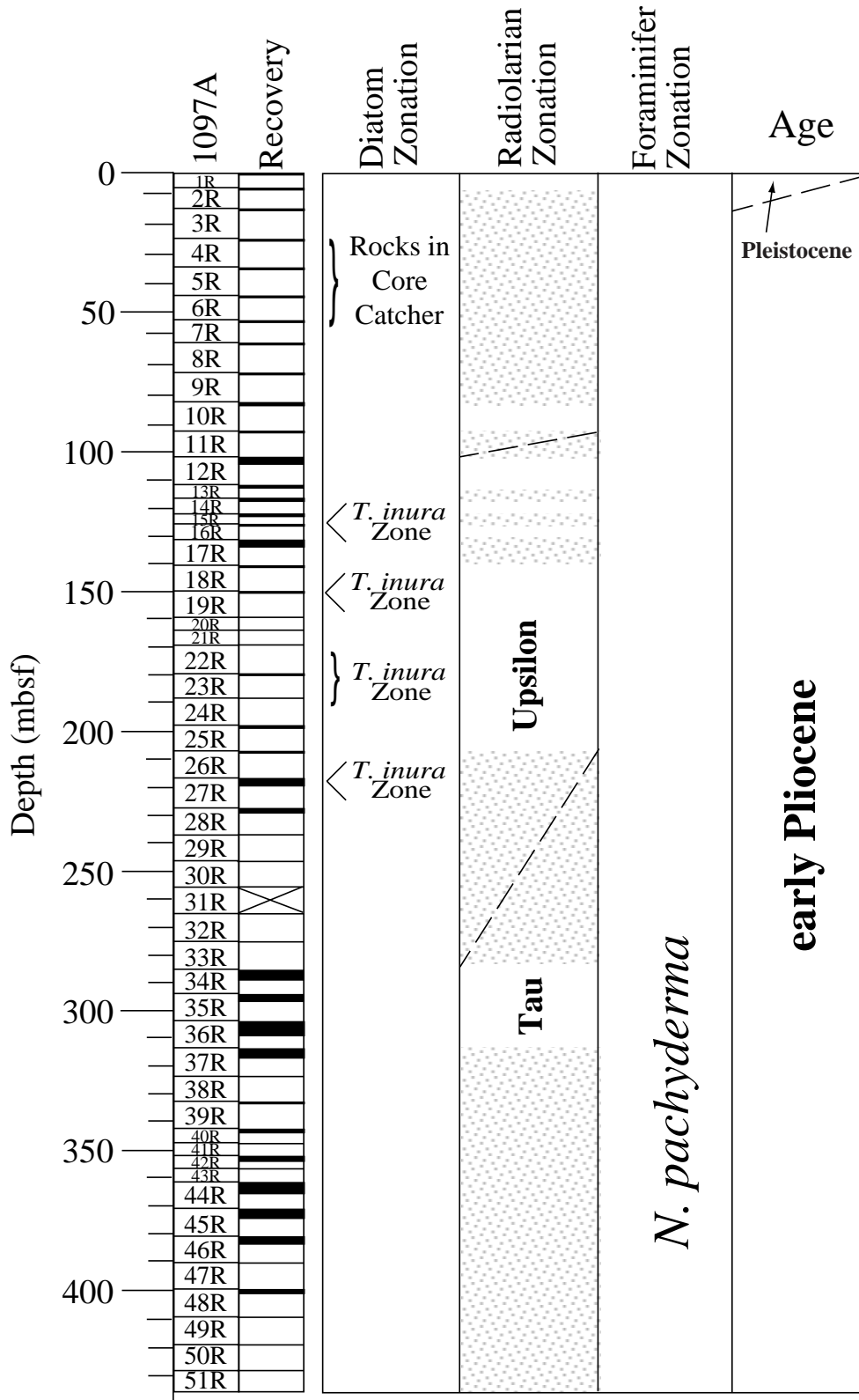
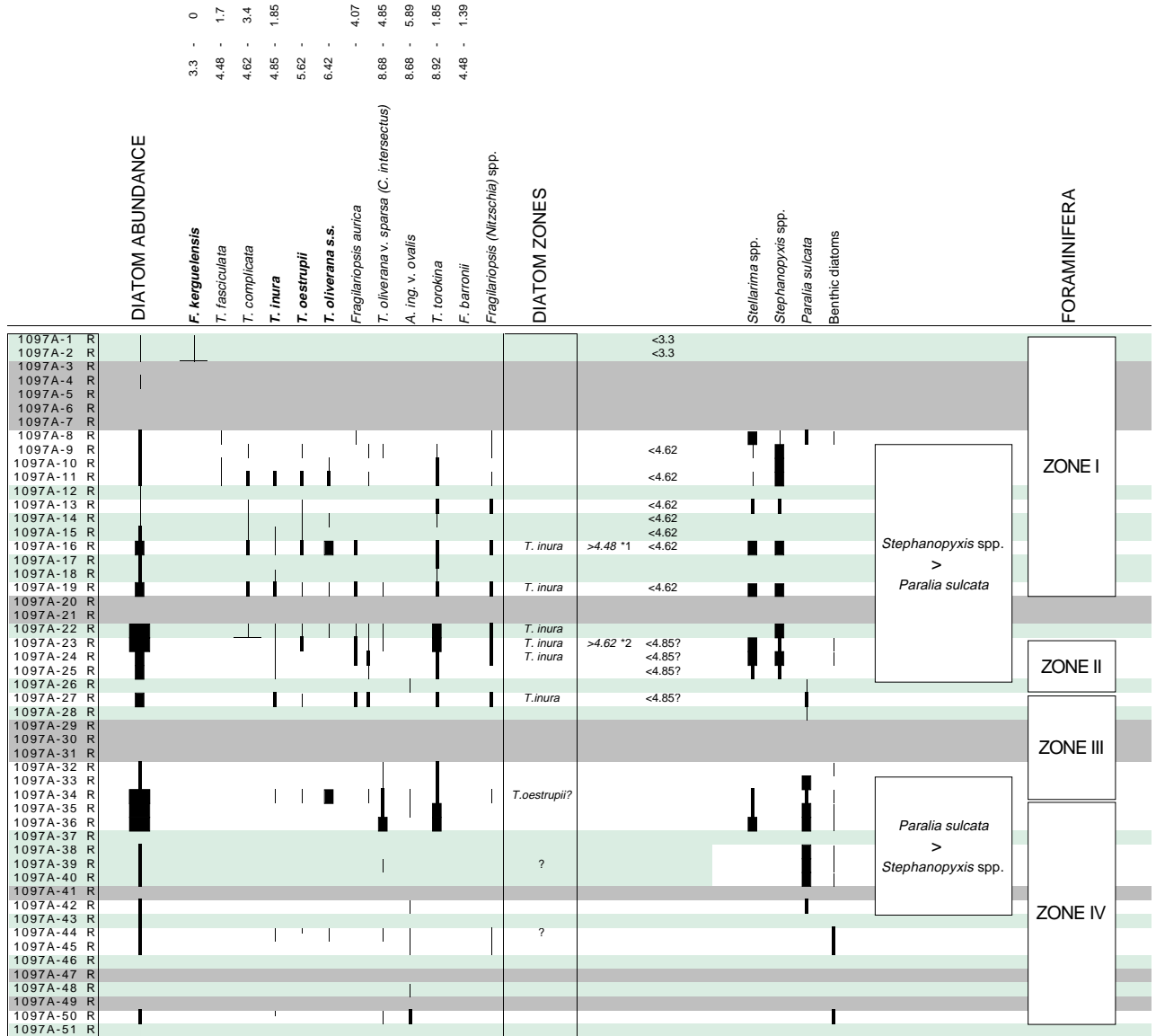


Figure F15. Diatom stratigraphy at Site 1097. On the left are total diatom abundance, the quantity of selected diatom species with depth, and diatom zonal assignments for certain samples; on the right are the abundance of selected diatoms recovered in smear slides, neritic and shelf diatom species assemblages (>20-µm slides), and benthic foraminifer zones. Dark gray bars = intervals with no fine sediment recovery; light gray bars = intervals of very rare occurrence of diatoms. *1 = The absence of *Fragilariopsis barronii* and presence of other *Fragilariopsis* species shows that there is a possibility of this age assignment. *2 = The absence of *Thalassiosira complicata* below this sample also shows a possible age assignment. A = abundant, C = common, F = frequent, R = rare, + = present.



A
C
F
R
+

Notes:

The abundance of total diatoms and age assignment species are based on smear-slide observation. The relative abundance of *Stellarima*, *Stephanopyxis*, and *Paralia sulcata* is mainly based on sieved (>20 µm) material. Light gray horizon shows observation based on poor slide condition, no sieved material, or very rare occurrence of diatoms. Dark gray shaded horizon indicates no fine sediment recovered. The first occurrence of *T. inura* (4.85 Ma; Harwood and Maruyama, 1991) is at an earlier age at Site 1095.

Figure F16. A. Inclination of the magnetization vector at the 30-mT demagnetization step from split cores (small \times 's) compared with mean inclinations obtained from principal component analysis of discrete samples (large circles). B. Maximum angular deviations obtained from principal component analysis of discrete samples. C. Intensity of remanence vs. depth after AF demagnetization at 30 mT.

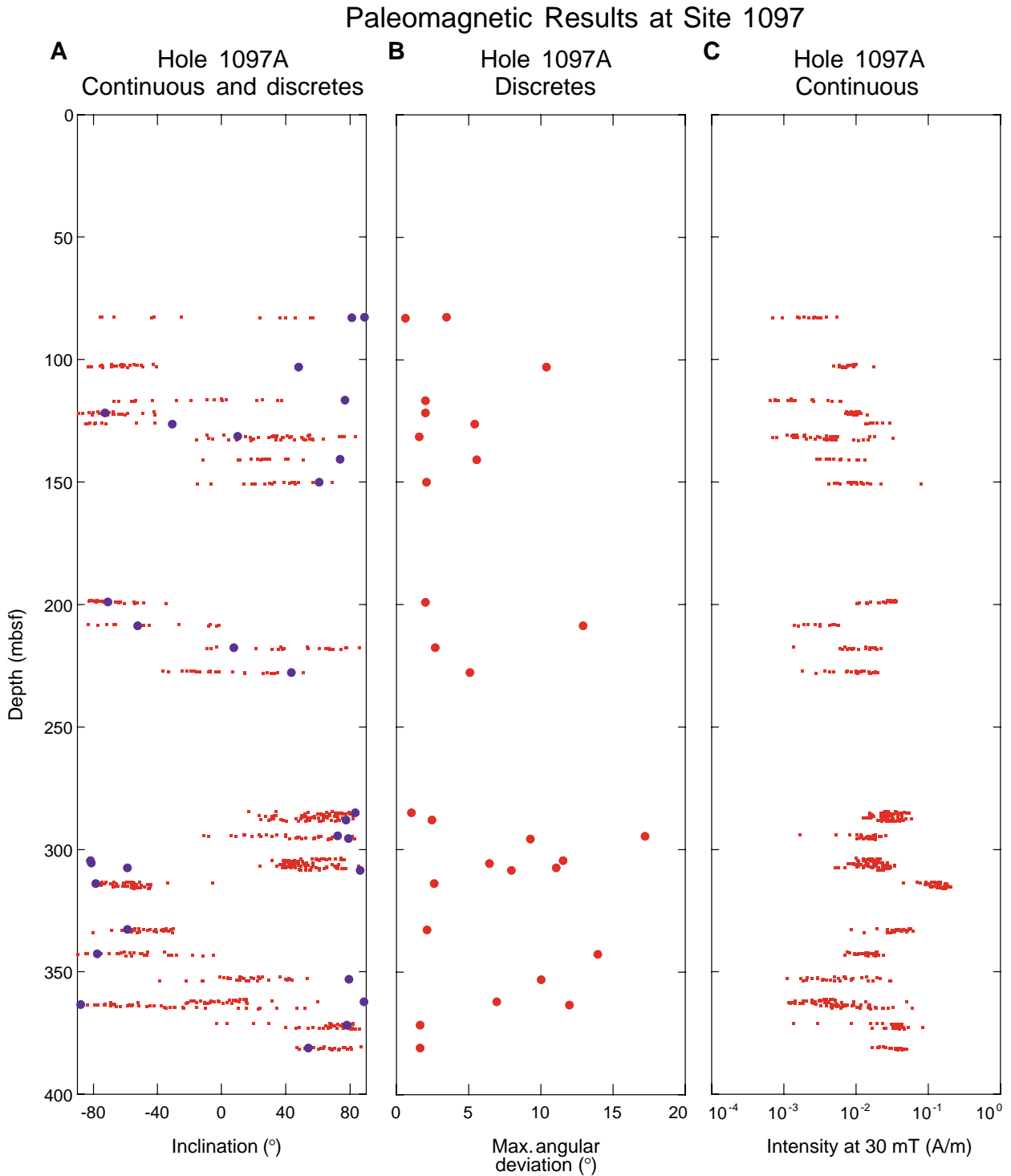


Figure F17. A. Orthogonal projection of the end-points of the remanence vector for Sample 178-1097A-15R-1, 53 cm. Open and solid symbols represent the vertical and horizontal projections, respectively. The drill-string overprint is removed at the 8-mT demagnetization step. B. Enlargement of boxed area in A, which shows that this sample has no stable direction of magnetization. C. Change in the intensity of remanence, normalized to the 0-mT (NRM) intensity, during AF demagnetization. D. Equal-area projection of the remanence vector during AF demagnetization.

Sample: 178-1097A-15R-1, 53.0 cm (121.63 mbsf)

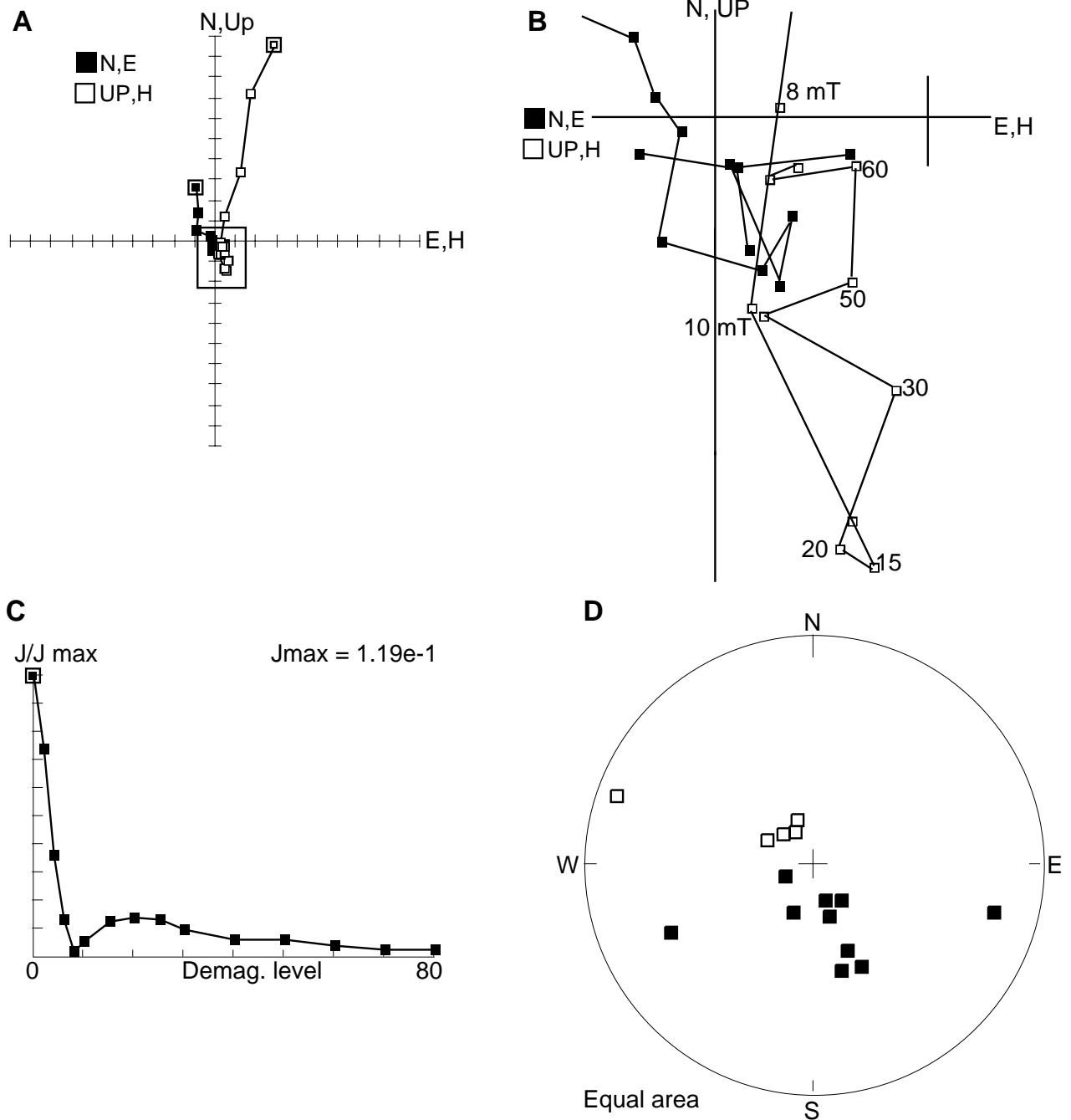


Figure F18. A. Orthogonal projection of the end-points of the remanence vector for Sample 178-1097A-27R-1, 34 cm. Open and solid symbols represent the vertical and horizontal projection, respectively. This sample has a shallow inclination. The direction becomes unstable at the 50-mT demagnetization step. B. Change in the intensity of remanence, normalized to the 0-mT (NRM) intensity, during AF demagnetization. C. Equal-area projection of the remanence vector during AF demagnetization.

Sample: 178-1097A-27R-1, 34.0 cm (217.64 mbsf)

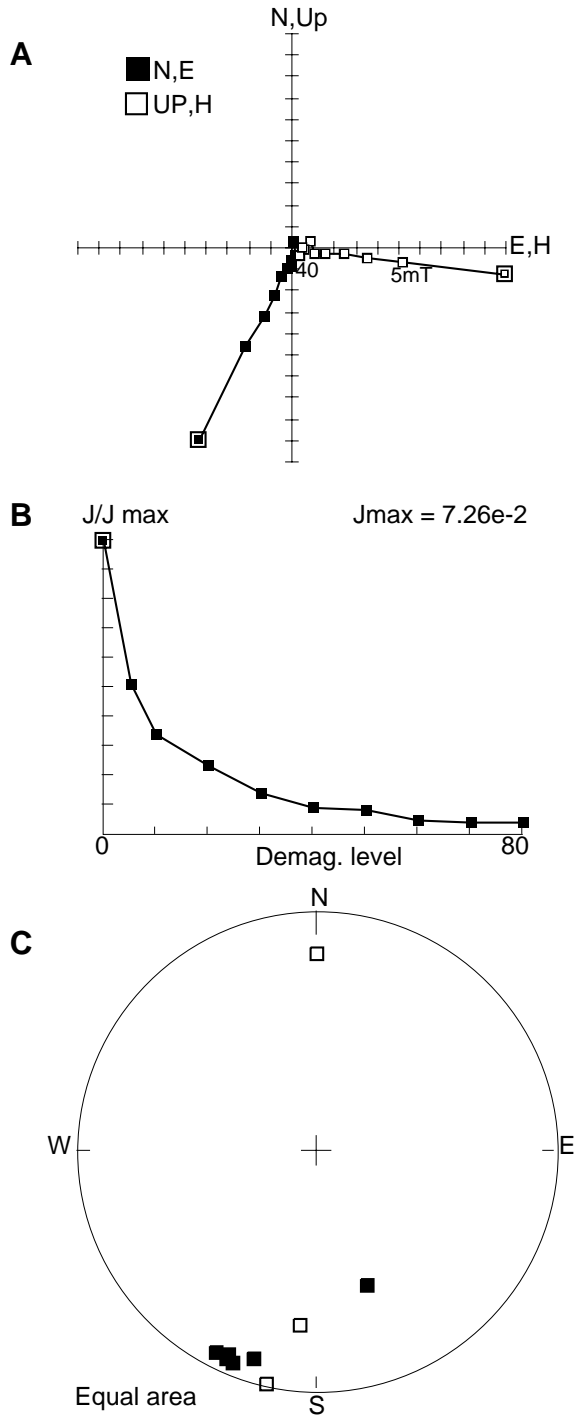


Figure F19. A. Orthogonal projection of the end-points of the remanence vector for Sample 178-1097A-25R-1, 77 cm. Open and solid symbols represent the vertical and horizontal projection, respectively. This sample displays the steep inclination expected for this site. B. Change in the intensity of remanence, normalized to the 0-mT (NRM) intensity, during AF demagnetization. C. Equal-area projection of the remanence vector during AF demagnetization.

Sample: 178-1097A-25R-1, 77.0 cm (198.87 mbsf)

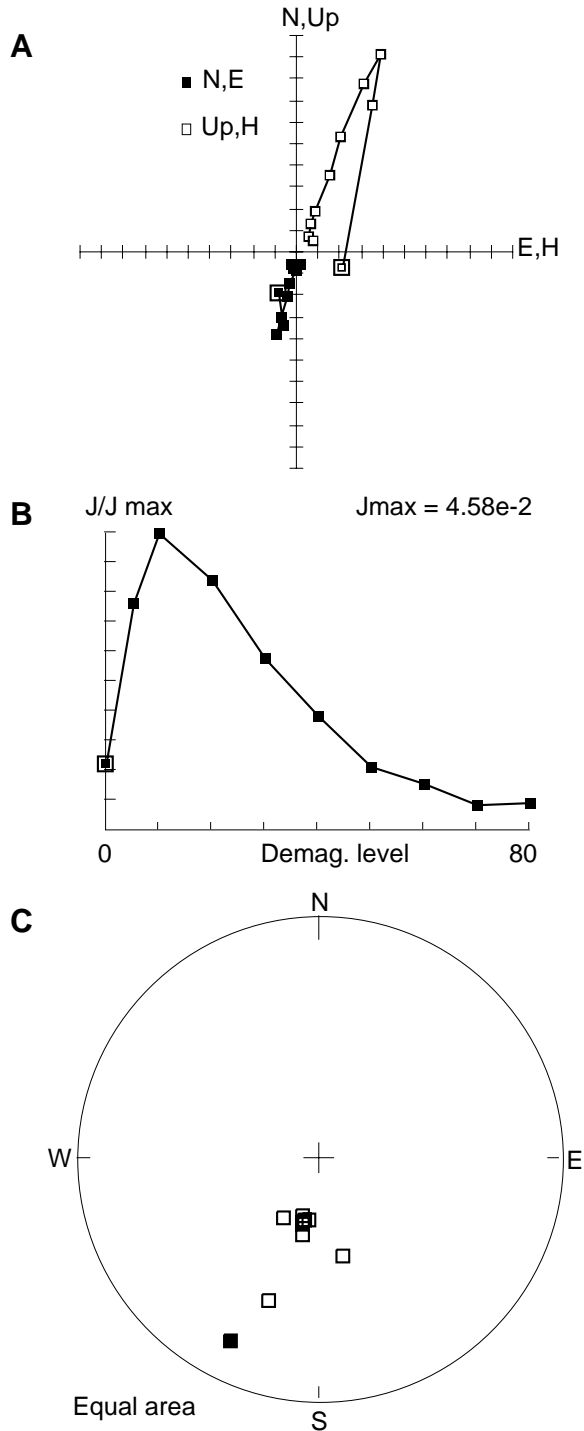


Figure F20. Calcium carbonate concentrations for Hole 1097A. Lithofacies are identified elsewhere on the basis of biostratigraphic and lithostratigraphic evidence (see “[Lithostratigraphy](#),” p. 3). Gray intervals have very low recovery.

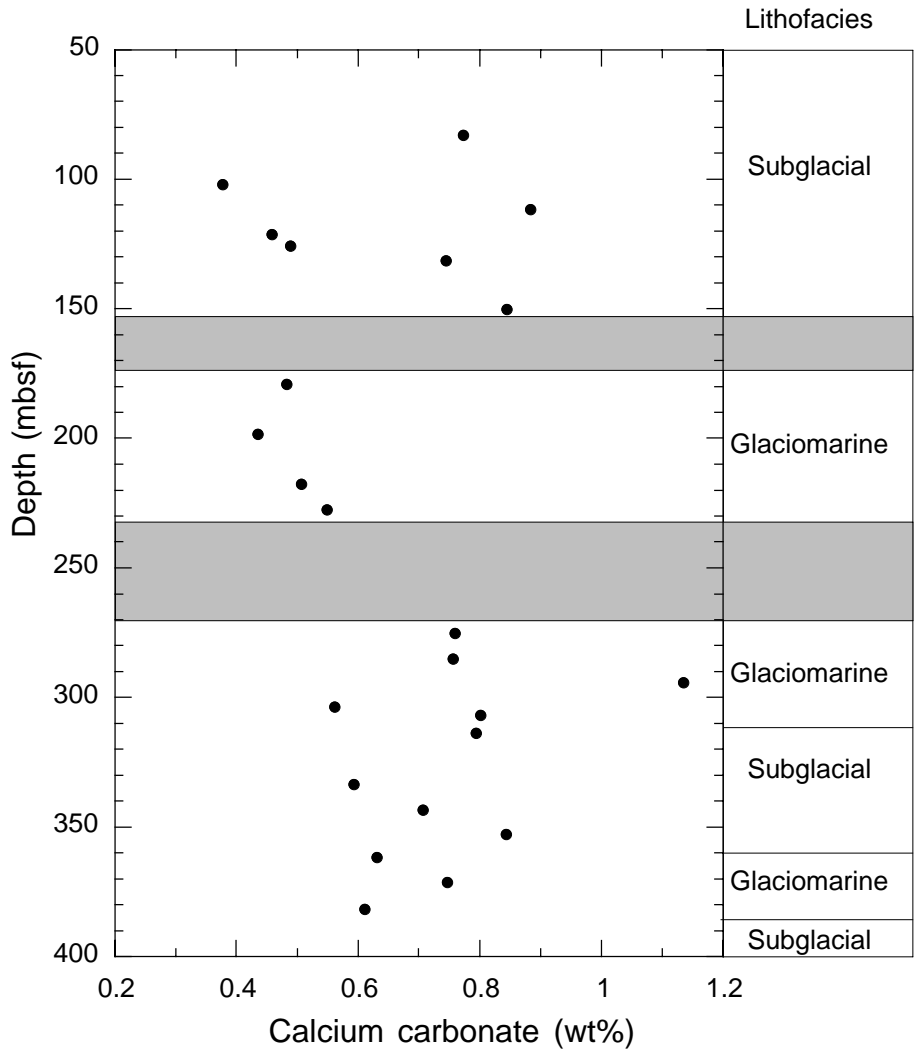


Figure F21. Profiles of interstitial water chemistry from Hole 1097A.

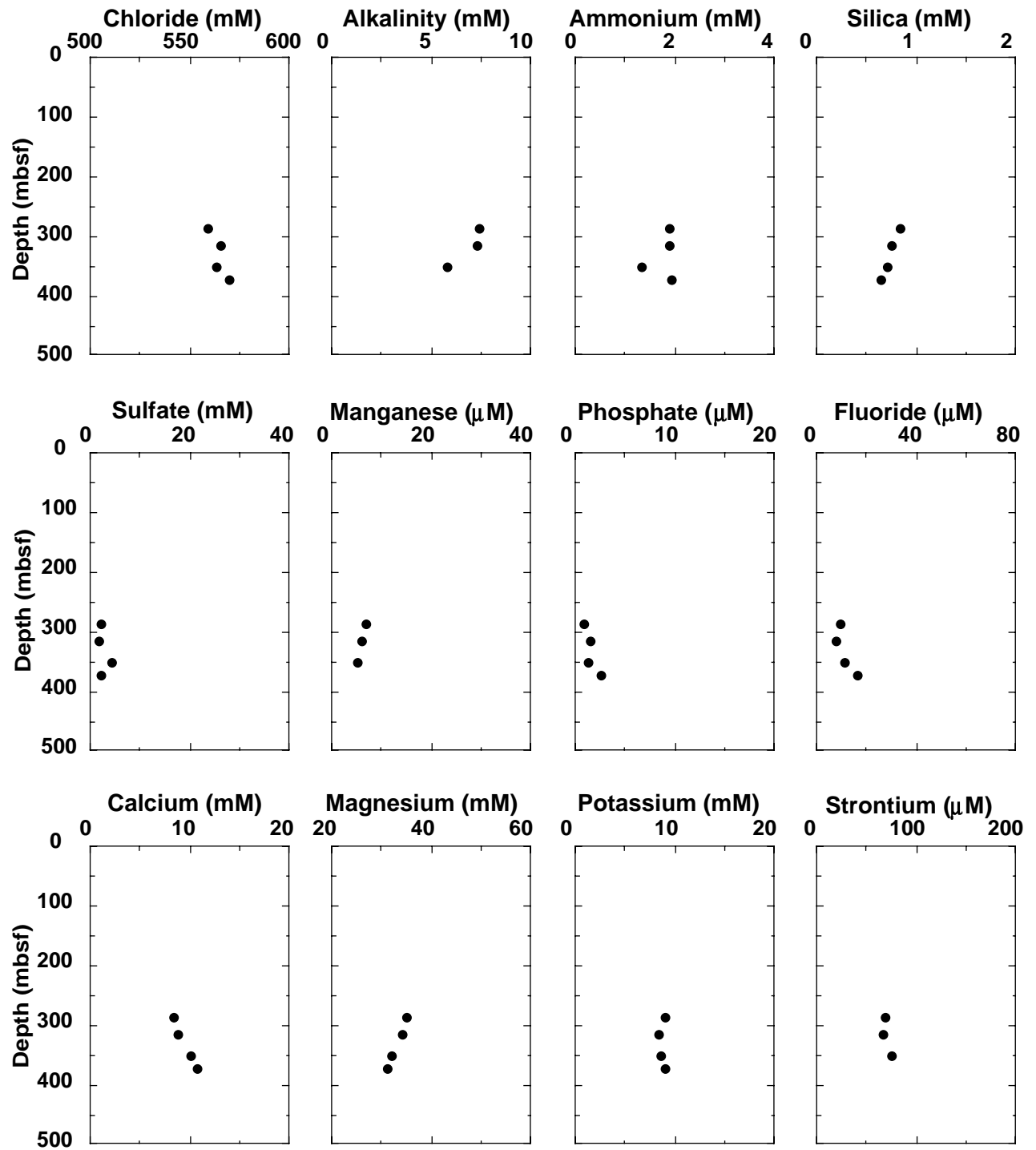


Figure F22. Ratios between X-ray diffraction intensities of selected peaks for chlorite (7 Å), illite (5 Å), and mixed-layer (~12 Å) clays in clay-sized sediment fractions from Site 1097. Peak height ratios do not reflect absolute concentrations.

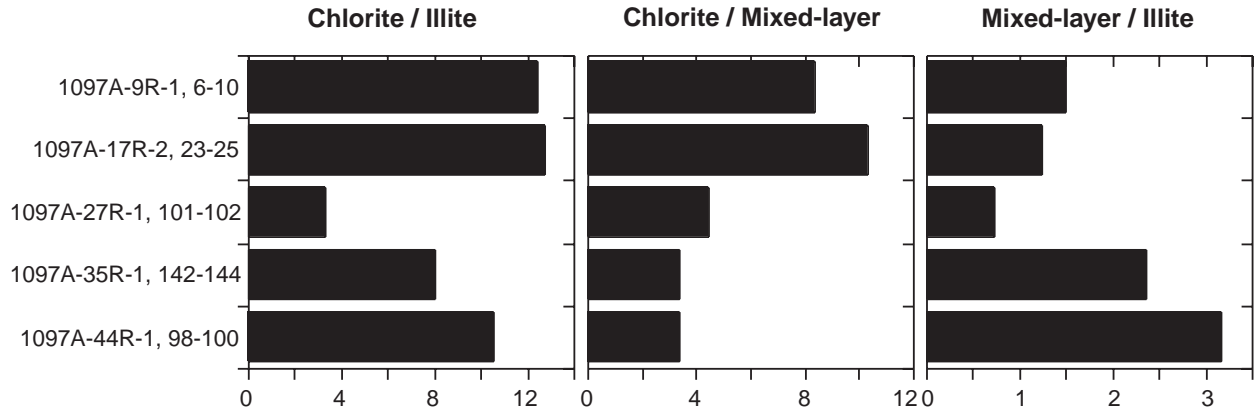


Figure F23. Raw data for (A) NGR, (B) GRAPE density, and (C) magnetic susceptibility. GRAPE data were truncated at 1.2 g/cm³, and susceptibility data were truncated at 0 to remove equipment noise.

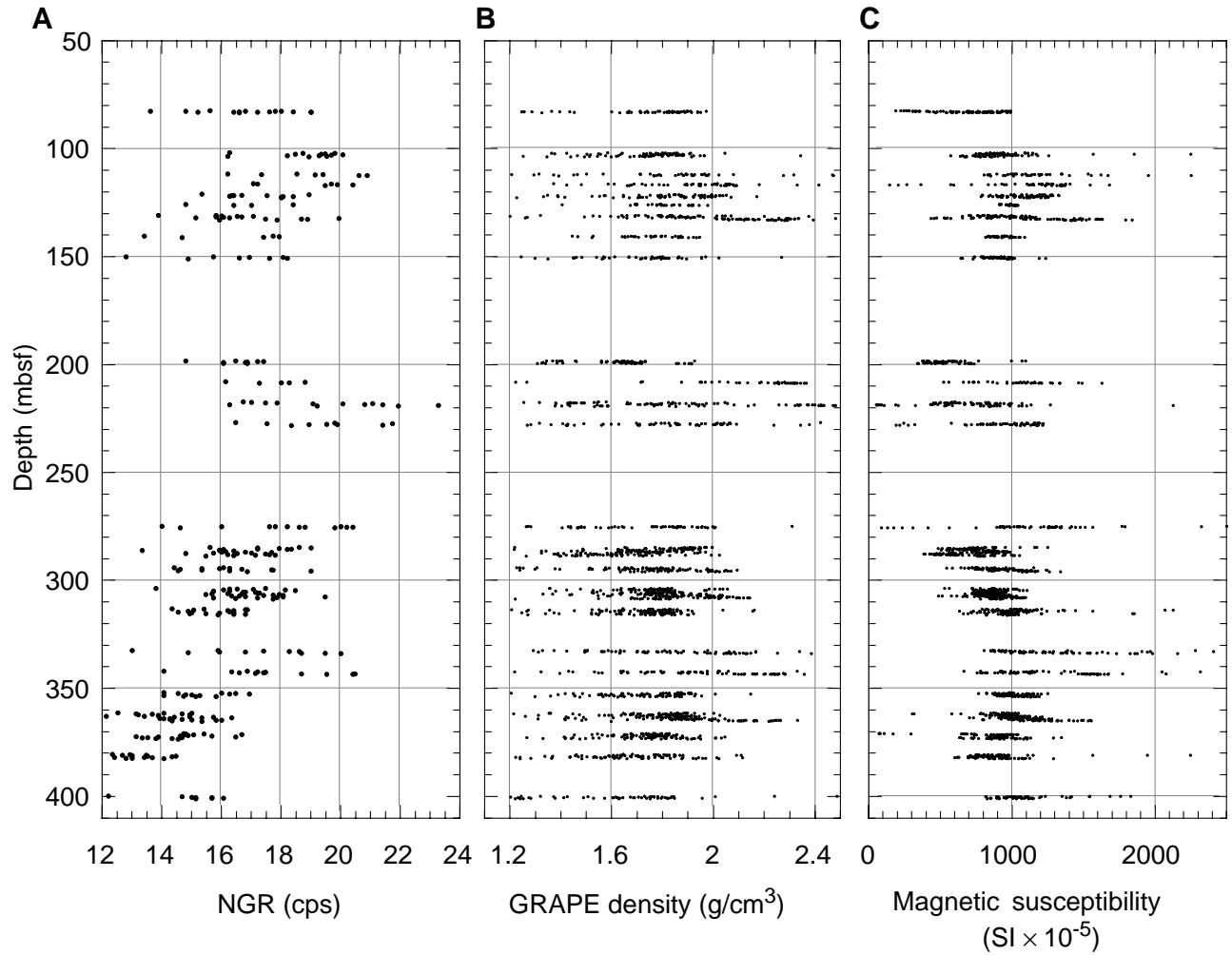


Figure F24. Index properties plots. A. Moisture and density (MAD) bulk density data (circles) and GRAPE bulk density (dots). B. Grain density. C. Porosity. Intervals suggested as subglacial (see "Lithostratigraphy," p. 3) are marked SG, and those interpreted as marine/glaciomarine are marked M.

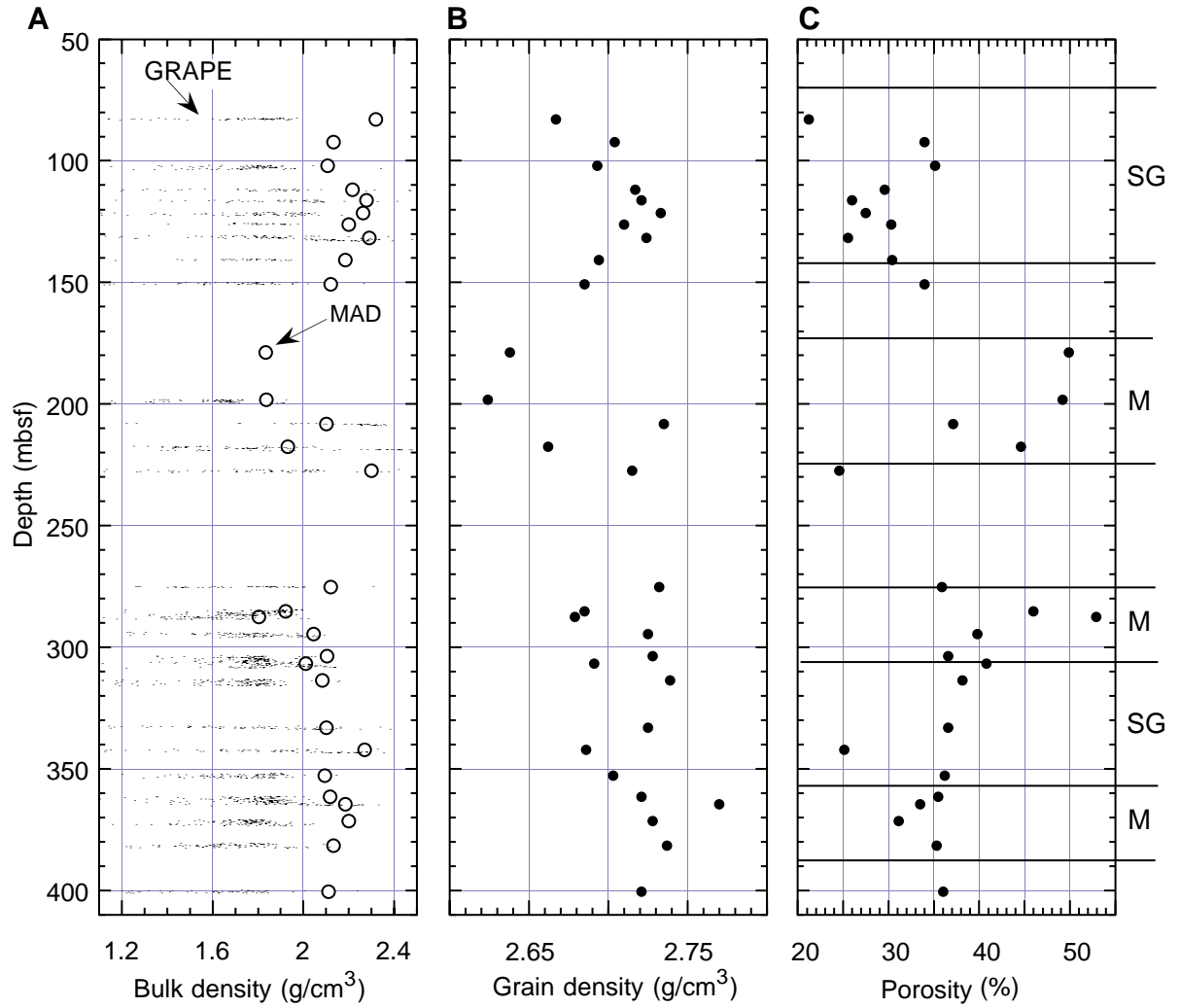


Figure F25. Magnetic susceptibility vs. natural gamma emission rates of sediments from the intervals interpreted as subglacial (see Fig. F24, p. 52). Crosses are from the lower subglacial sequence; open squares are from the upper subglacial sequence

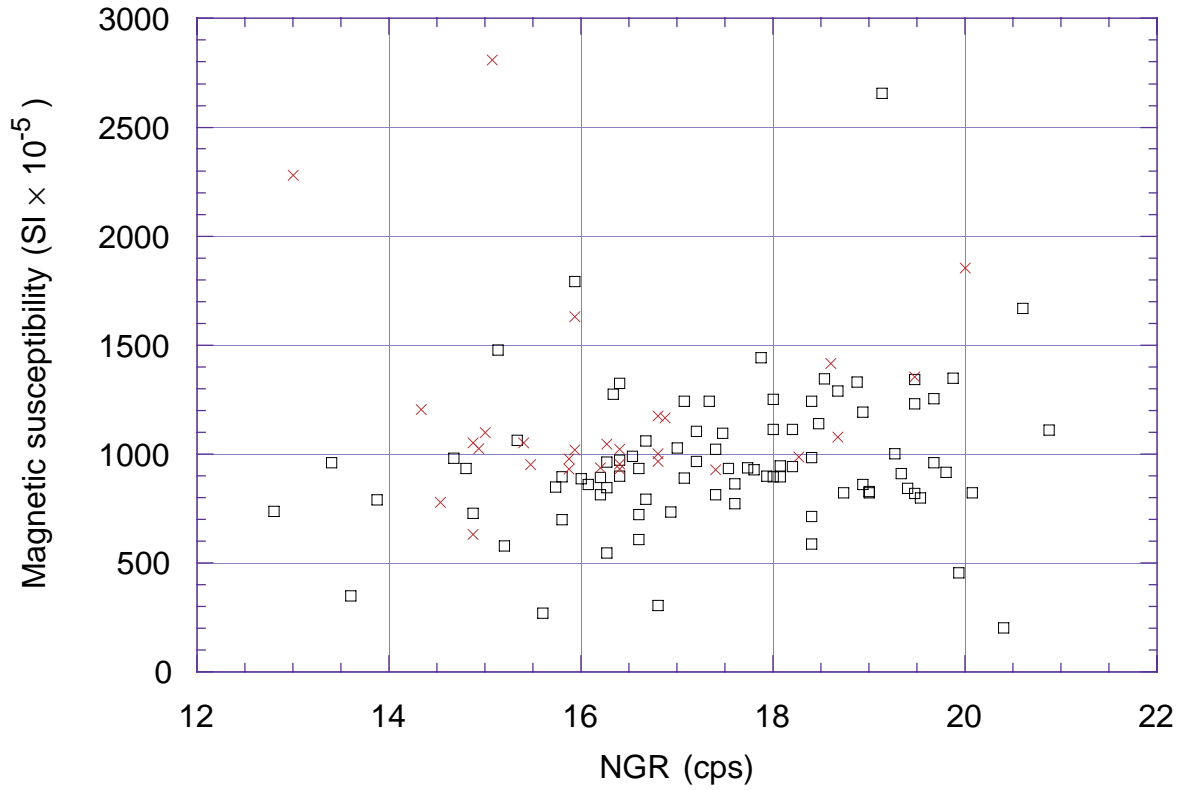


Figure F26. Comparison of (A) PWS3 velocity and (B) MAD bulk density.

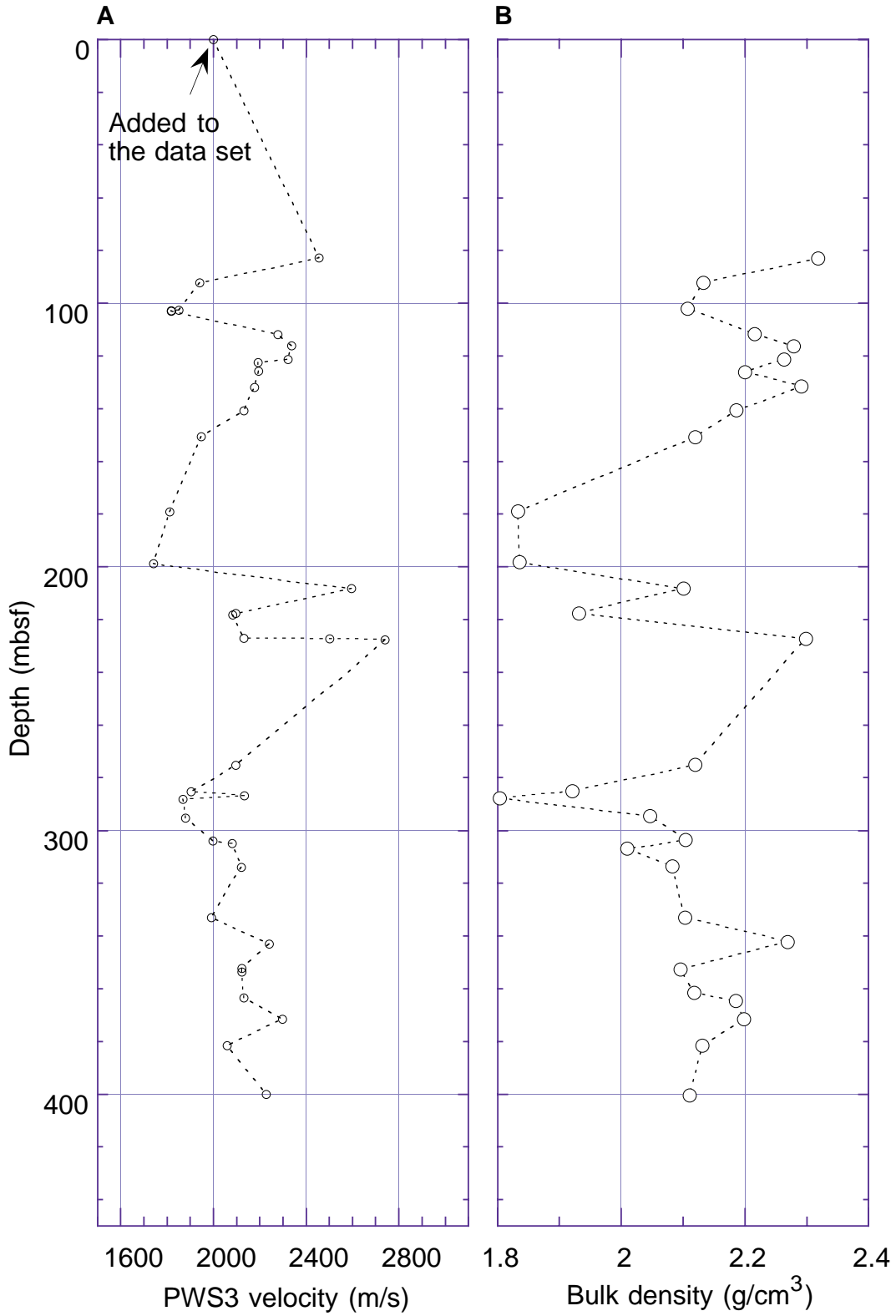


Figure F27. Photomicrograph of Sample 178-1097A-25R-1, 91 cm (plane-polarized light), a laminated diamict, at 10:1 magnification.

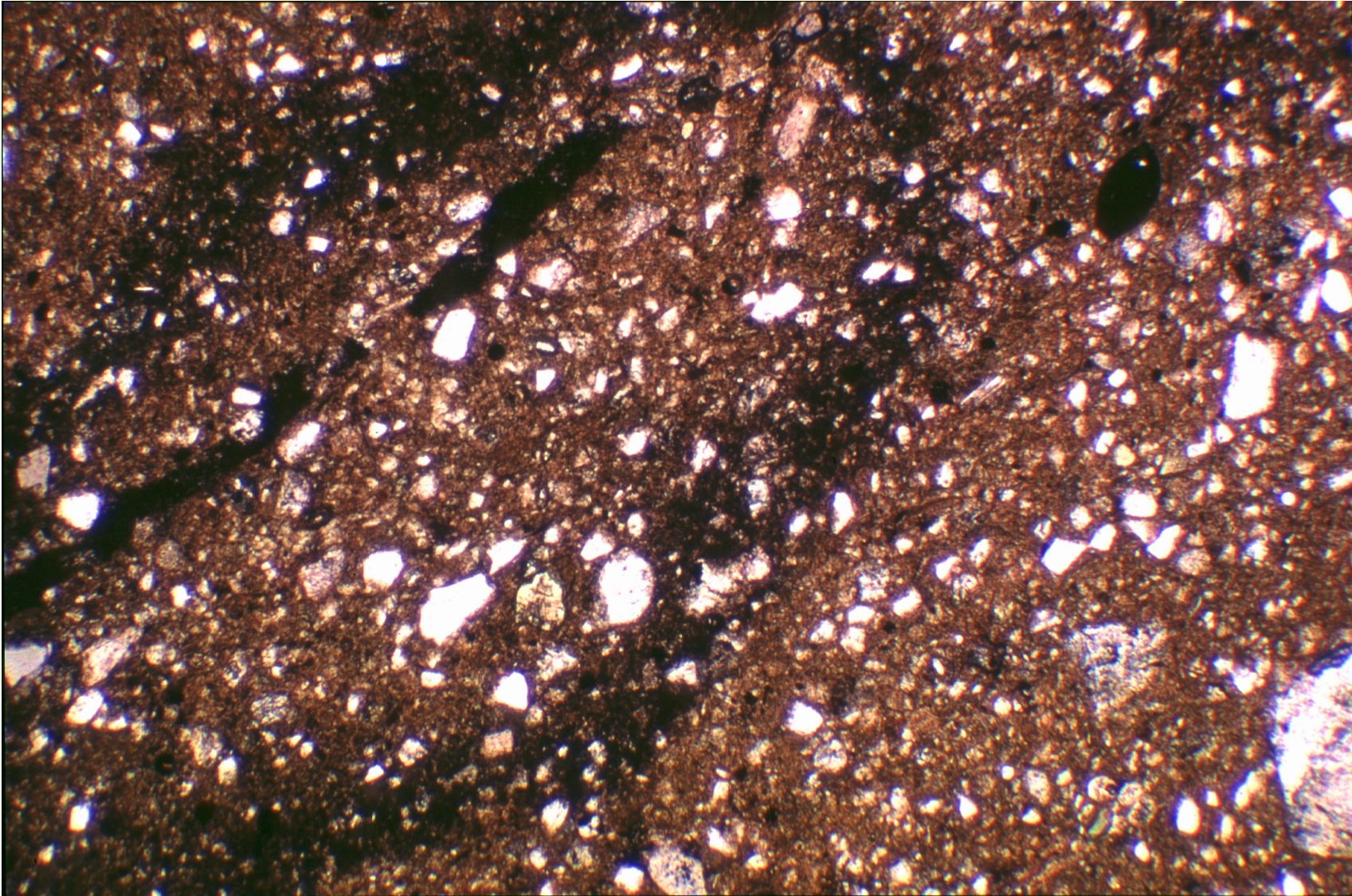


Figure F28. Multichannel seismic profile AISM-06 across Site 1097, located in Figure F2B, p. 25, with seismic Units I, II, and III. MSH = mid-shelf high, S.P. = shotpoint.

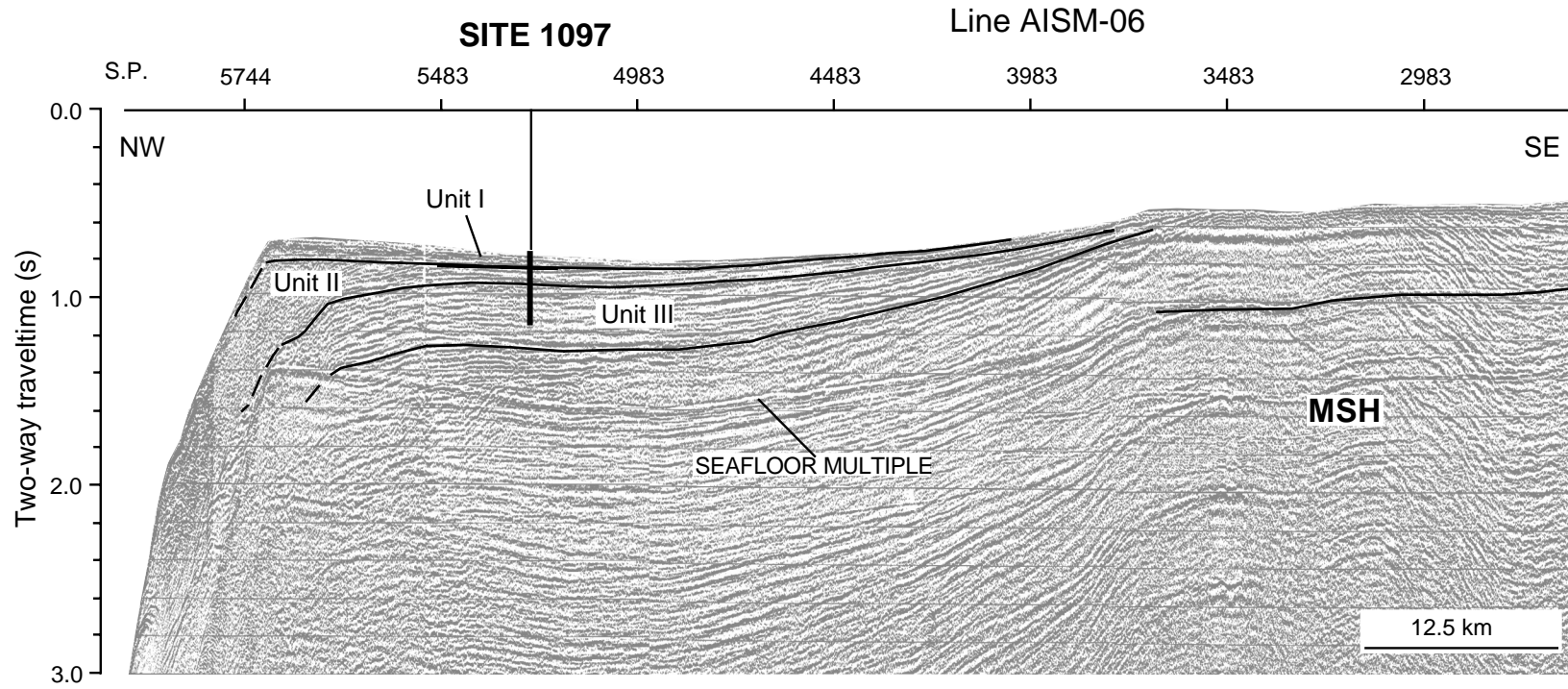


Figure F29. Detail of multichannel seismic profile AISM-06 across Site 1097. S.P. = shotpoint.

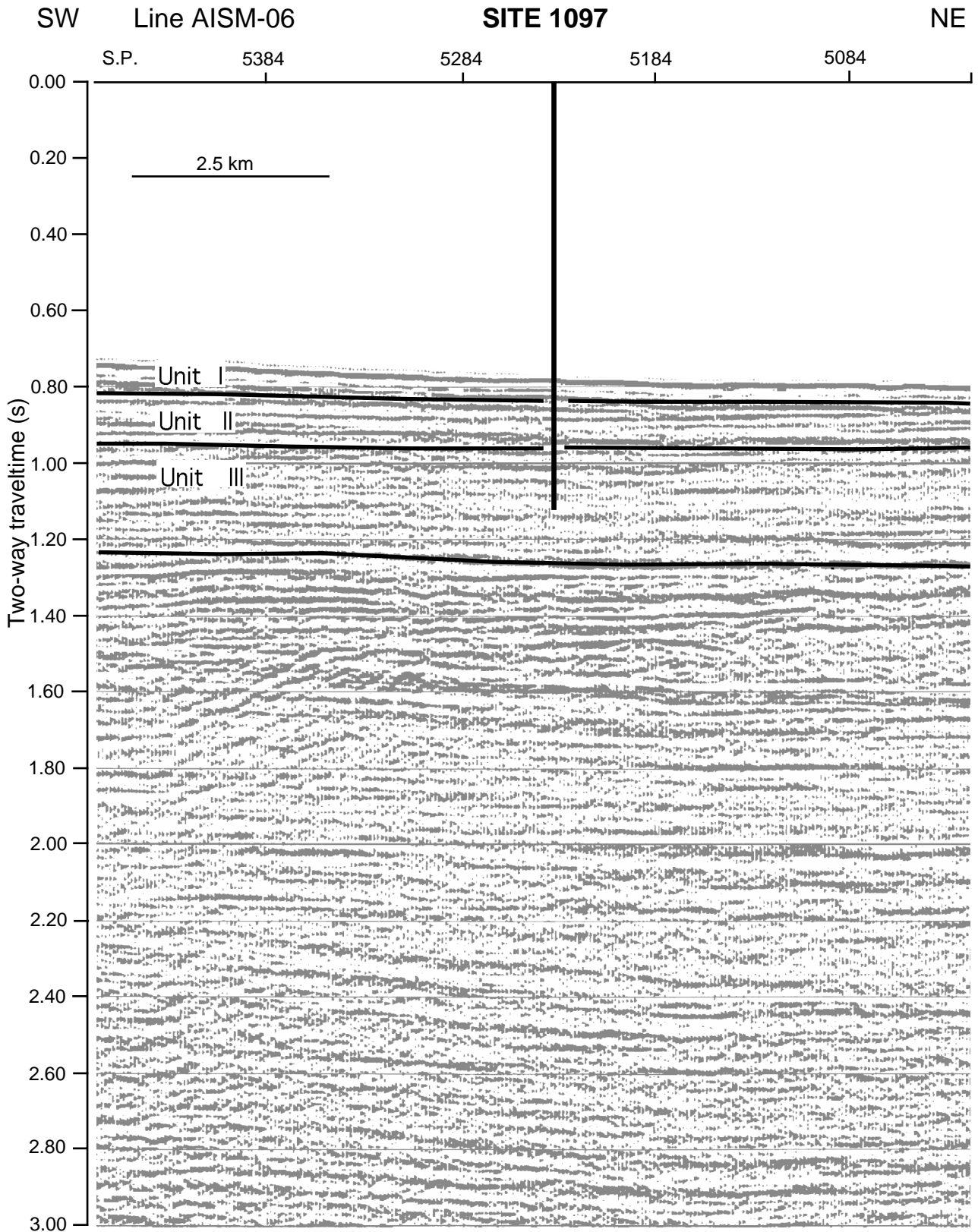


Figure F30. Traveltime-depth function and correlation between physical properties and seismic units. The use of the smooth velocity curve in determining the traveltime-depth relation involves several assumptions that cannot be considered in detail here. The curve is not suitable for generation of a synthetic seismogram. For details of the smooth density curve, see "Physical Properties," p. 15. PWS3 Hamilton Frame equipment.

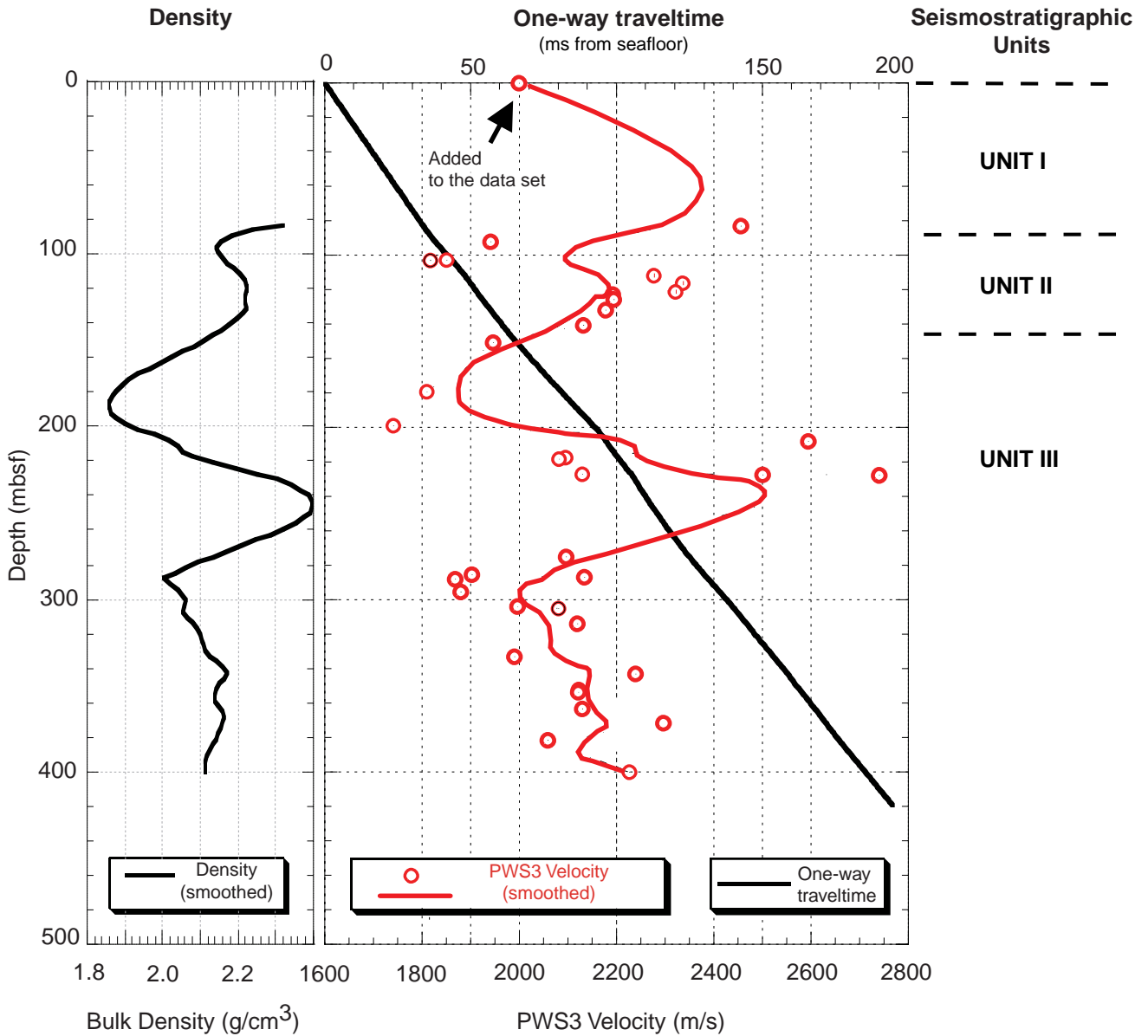


Table T1. Site 1097 coring summary.

Core	Date (March 1998)	Time (UTC)	Depth (mbsf)	Length cored (m)	Length recovered (m)	Recovery (%)
178-1097A-						
1R	6	1125	0.0-7.5	7.5	0.1	0.9
2R	6	1455	7.5-15.4	7.9	0.0	0.5
3R	6	1830	15.4-25.0	9.6	0.2	1.7
4R	6	2025	25.0-34.6	9.6	0.6	6.8
5R	6	2140	34.6-44.2	9.6	0.4	4.2
6R	6	2250	44.2-53.6	9.4	0.3	3.5
7R	7	0010	53.6-63.2	9.6	0.0	0.0
8R	7	0340	63.2-72.8	9.6	0.2	1.9
9R	7	0545	72.8-82.4	9.6	0.5	5.3
10R	7	0820	82.4-92.1	9.7	1.1	11.0
11R	7	0940	92.1-101.8	9.7	0.4	4.6
12R	7	1100	101.8-111.5	9.7	2.1	21.6
13R	7	1300	111.5-116.1	4.6	1.2	25.9
14R	7	1450	116.1-121.1	5.0	1.2	23.6
15R	7	1625	121.1-125.7	4.6	1.8	38.5
16R	7	1735	125.7-130.7	5.0	0.7	14.6
17R	7	2040	130.7-140.3	9.6	2.7	28.0
18R	7	2230	140.3-149.9	9.6	1.0	10.0
19R	7	2350	149.9-159.5	9.6	1.2	12.8
20R	8	0300	159.5-164.1	4.6	0.2	4.8
21R	8	0240	164.1-169.2	5.1	0.0	1.0
22R	8	0335	169.2-178.9	9.7	0.2	1.5
23R	8	0435	178.9-188.5	9.6	0.8	8.3
24R	8	0545	188.5-198.1	9.6	0.2	2.4
25R	8	0650	198.1-207.7	9.6	1.8	18.8
26R	8	0930	207.7-217.3	9.6	1.2	13.0
27R	8	1215	217.3-226.9	9.6	2.1	22.3
28R	8	1445	226.9-236.6	9.7	1.4	14.7
29R	8	1550	236.6-246.2	9.6	0.2	1.6
30R	9	1350	246.2-255.7	9.5	0.2	1.8
31R	9	1615	255.7-265.3	9.6	0.2	2.2
32R	9	1710	265.3-274.9	9.6	0.3	2.7
33R	9	1820	274.9-284.5	9.6	0.8	8.0
34R	9	1915	284.5-293.9	9.4	4.3	46.2
35R	9	2140	293.9-303.5	9.6	2.4	24.5
36R	9	2230	303.5-313.1	9.6	5.3	55.6
37R	9	2320	313.1-322.7	9.6	3.1	32.3
38R	10	0025	322.7-332.3	9.6	0.2	1.9
39R	10	0130	332.3-341.9	9.6	1.8	18.6
40R	10	0300	341.9-346.9	5.0	1.9	38.6
41R	10	0440	346.9-351.5	4.6	0.3	5.7
42R	10	1600	351.5-356.5	5.0	2.4	47.8
43R	10	1715	356.5-361.2	4.7	0.3	5.5
44R	10	2000	361.2-370.8	9.6	4.2	44.2
45R	10	2130	370.8-380.5	9.7	2.8	29.1
46R	10	2250	380.5-390.2	9.7	2.3	23.3
47R	11	0030	390.2-399.8	9.6	0.2	2.4
48R	11	0135	399.8-409.4	9.6	1.5	15.5
49R	11	0250	409.4-419.0	9.6	0.2	1.6
50R	11	0430	419.0-428.6	9.6	0.7	7.2
51R	11	0530	428.6-436.6	8.0	0.1	1.8
Coring totals:				436.6	59.3	13.6

Notes: UTC = Universal Time Coordinated. An expanded version of this coring summary table that includes lengths and depths of sections and comments on sampling is included in ASCII format in the [TABLES](#) directory.

Table T2. Benthic foraminiferal biofacies of shipboard samples from Site 1097.

Core, section, interval (cm)	Depth (mbsf)	Biofacies A predominantly reworked	Biofacies B low saline/ sedimentation dilution	Biofacies C shallow marine	Zone
178-1097A-					
1R-CC, 0-2	0	X			
2R-CC, 0-4	7.5	X			
8R-CC, 10-12	63.3	X			
9R-1W, 48-51	73.28	X			
10R-CC, 12-16	83.36	X			
12R-CC, 10-15	103.85	X			
13R-CC, 7-17	112.59	X			Zone I
14R-CC, 12-17	117.23	X			
15R-CC, 9-14	122.82	X			
16R-CC, 10-12	126.41	X			
17R-CC, 20-25	133.34	X			
18R-CC, 10-15	141.21	X			
19R-CC, 6-11	151.08	X			
23R-1W, 42-44	179.32			X	
24R-CC, 18-23	188.68			X	
25R-1W, 22-23	198.32	B			Zone II
25R-1W, 147-151	199.57	X			
26R-CC, 22-26	208.91		X		
27R-1W, 99-101	218.29	X			
27R-2W, 72-75	219.25	B			
28R-CC, 9-14	228.28	X			Zone III
32R-CC, 26-28	265.56	X			
34R-3W, 20-22	287.7	B			
34R-CC, 9-14	288.79		X		
35R-1W, 100-101	294.9			X	
35R-CC, 24-29	296.2	X			
36R-2W, 85-87	305.8			X	
36R-CC, 20-25	308.79			X	
37R-CC, 15-20	316.15	B			
39R-CC, 16-18	334.02	X			
40R-CC, 21-26	343.78		X		Zone IV
42R-CC, 5-7	353.97	X			
44R-2W, 35-37	363.05		X		
44R-CC, 21-26	365.39			X	
45R-CC, 12-15	373.59		X		
46R-CC, 10-14	382.72		X		
48R-CC, 10-11	401.22	X			
50R-CC, 10-12	419.82	X			

Note: B = samples barren of foraminifers, X = placement of the sample in a particular biofacies.

Table T3. Volatile hydrocarbons measured at Site 1097.

Core, section, interval (cm)	Depth (mbsf)	Methane (ppm)	Ethane (ppm)	Ethylene (ppm)	Propane (ppm)	Methane/ Ethane
178-1097A-						
17R-2, 103-106	133.11	1,520	0.0	0.0	0.0	
18R-1, 80-81	141.10	47,600	6.5	1.0	0.0	7,300
19R-1, 111-112	151.01	3,970	0.0	0.0	0.0	
23R-1, 0-2	178.90	76,100	8.7	0.9	0.7	8,700
25R-1, 0-5	198.10	61,500	6.0	0.8	0.0	10,000
26R-2, 74-79	208.64	8,230	1.6	0.8	0.0	5,100
34R-2, 0-2	286.00	22,600	5.9	0.0	1.1	3,800
35R-2, 54-56	295.94	44,000	7.2	0.0	0.9	6,100
36R-3, 0-2	306.50	52,700	9.8	0.0	1.4	5,400
37R-2, 0-2	314.60	58,400	10.0	0.0	1.0	5,800
39R-2, 60-61	333.90	17,900	5.1	0.0	1.0	3,500
40R-1, 0-2	341.90	24,700	4.7	0.0	0.5	5,300
42R-2, 114-115	353.06	6,210	2.6	0.0	0.0	2,400
44R-3, 0-3	364.20	27,800	6.7	0.0	1.0	4,200
45R-2, 0-2	372.30	69,900	14.2	0.0	1.9	4,900
46R-2, 0-2	382.00	43,000	11.4	1.1	2.6	3,800
48R-1, 131-132	401.11	35,000	8.4	0.0	2.2	4,200

Table T4. Summary of inorganic carbon, carbonate, and elemental analyses for Hole 1097A.

Core, section, interval (cm)	Depth (mbsf)	IC (wt%)	CaCO ₃ (wt%)	TOC (wt%)	TC (wt%)	TN (wt%)	TS (wt%)
178-1097A-							
10R-1, 57-58	82.97	0.09	0.77				
12R-1, 19-20	101.99	0.05	0.38				
13R-1, 22-23	111.72	0.11	0.88				
15R-1, 26-27	121.36	0.06	0.46				
16R-1, 9-10	125.79	0.06	0.49				
17R-1, 88-89	131.58	0.09	0.74				
19R-1, 28-29	150.18	0.10	0.84				
23R-1, 21-22	179.11	0.06	0.48	0.50	0.56	0.05	0.32
25R-1, 15-16	198.25	0.05	0.43	0.61	0.66	0.05	0.23
27R-1, 28-29	217.58	0.06	0.51	0.46	0.52	0.05	0.12
28R-1, 62-63	227.52	0.07	0.55				
33R-1, 24-25	275.14	0.09	0.76				
34R-1, 58-59	285.08	0.09	0.76				
35R-1, 35-36	294.25	0.14	1.13	0.28	0.42	0.05	0.46
36R-1, 9-11	303.59	0.07	0.56	0.21	0.27	0.03	0.23
36R-3, 27-29	306.77	0.10	0.80	0.16	0.26	0.07	0.26
37R-1, 79-80	313.89	0.10	0.79				
39R-2, 26-27	333.56	0.07	0.59				
40R-2, 40-41	343.30	0.08	0.71				
42R-2, 84-85	352.76	0.10	0.84				
44R-1, 37-38	361.57	0.08	0.63	0.16	0.23	0.05	0.29
45R-1, 41-42	371.21	0.09	0.75	0.23	0.32	0.02	0.23
46R-1, 117-118	381.67	0.07	0.61	0.16	0.24	0.03	0.26

Note: IC = inorganic carbon, CaCO₃ = calcium carbonate, TOC = total organic carbon, TC = total carbon, TN = total nitrogen, and TS = total sulfur.

Table T5. Results of interstitial water analyses for Hole 1097A.

Core, section, interval (cm)	Depth (mbsf)	pH	Salinity	Cl ⁻ (mM)	Alkalinity (mM)	NH ₄ ⁺ (mM)	Si(OH) ₄ (mM)	SO ₄ ²⁻ (mM)	Mn ²⁺ (μM)	Fe ²⁺ (μM)	PO ₄ ³⁻ (μM)	F ⁻ (μM)	Ca ²⁺ (mM)	Mg ²⁺ (mM)	K ⁺ (mM)	Sr ²⁺ (μM)
178-1097A-																
34R-2, 140-150	287.40	8.0	32	559	7.4	1.87	0.84	2.2	7	0.3	0.8	9.5	8.4	35.2	8.9	68
37R-1, 140-150	314.50	8.2	32	565	7.3	1.87	0.74	1.8	6	2.3	1.6	7.6	8.8	34.1	8.4	66
42R-2, 114-124	353.06	8.2	32	563	5.8	1.34	0.72	4.3	5	—	1.2	11.2	10.0	31.9	8.5	74
45R-1, 140-150	372.20	—	32	570	—	1.93	0.64	2.2	—	—	2.6	16.1	10.8	31.1	9.1	—

Note: — = no analysis.

Table T6. Relative intensities of selected X-ray diffraction peaks from bulk mineral samples of Site 1097 sediments.

Core, section, interval (cm)	Depth (mbsf)	Chlorite (7 Å)	Quartz (3.34 Å)	Plagioclase (3.19 Å)
178-1097A-				
9R-1, 6-10	72.86	9	100	54
17R-2, 23-25	132.31	9	100	75
27R-1, 101-102	218.31	13	100	43
35R-1, 142-144	295.32	7	100	81
44R-1, 98-100	362.18	7	100	77

Note: Highest selected peak intensity is normalized to 100.

Table T7. Relative intensities of selected X-ray diffraction peaks from clay mineral samples of Site 1097 sediments.

Core, section, interval (cm)	Depth (mbsf)	Chlorite (7 Å)	Illite (5 Å)	Mixed layer (~12 Å)
178-1097A-				
9R-1, 6-10	72.86	100	8	12
17R-2, 23-25	132.31	100	8	10
27R-1, 101-102	218.31	100	31	22
35R-1, 142-144	295.32	100	12	30
44R-1, 98-100	362.18	100	9	30

Note: Highest selected peak intensity is normalized to 100.

Table T8. Trace-element chemistry of bulk sediment in Hole 1097A.

Core, section, interval (cm)	Depth (mbsf)	Nb (ppm)	Zr (ppm)	Y (ppm)	Sr (ppm)	Rb (ppm)	Zn (ppm)	Cu (ppm)	Ni (ppm)	Cr (ppm)	V (ppm)	Ce (ppm)	Ba (ppm)
178-1097A-													
9R-1, 6-10	72.86	8	159	25	323	56	81	30	21	25	148	31	379
17R-2, 23-25	132.31	8	150	21	315	49	67	22	18	23	129	44	361
27R-1, 101-102	218.31	11	131	26	261	63	98	30	25	30	145	31	309
35R-1, 142-144	295.32	10	161	23	326	56	73	23	19	25	147	51	385
44R-1, 98-100	362.18	10	161	23	350	53	72	27	17	23	145	45	345